J Physiol 600.14 (2022) pp 3355–3381

The Journal of Physiology

Connectivity and synaptic features of hilar mossy cells and their effects on granule cell activity along the hippocampal longitudinal axis

Wahab Imam Abdulmajeed[1,2,3], Kai-Yi Wang[2], Jei-Wei Wu[2], Musa Iyiola Ajibola[1,2], Irene Han-Juo Cheng[1,4,5] and Cheng-Chang Lien[1,2,5]

[1] *Taiwan International Graduate Program in Interdisciplinary Neuroscience, Academia Sinica, Taipei, Taiwan*
[2] *Institute of Neuroscience, National Yang Ming Chiao Tung University, Taipei, Taiwan*
[3] *Department of Physiology, Faculty of Basic Medical Sciences, College of Health Sciences, University of Ilorin, Ilorin, Nigeria*
[4] *Institute of Brain Science, National Yang Ming Chiao Tung University, Taipei, Taiwan*
[5] *Brain Research Center, National Yang Ming Chiao Tung University, Taipei, Taiwan*

Edited by: Katalin Toth & Jean-Claude Béïque

The peer review history is available in the Supporting Information section of this article (https://doi.org/10.1113/JP282804#support-information-section).

[Correction made on 15 July 2022, after first online publication: In the graphical abstract, 'intralamellar' was incorrectly presented as 'intranalamellar'. This has since been corrected.]

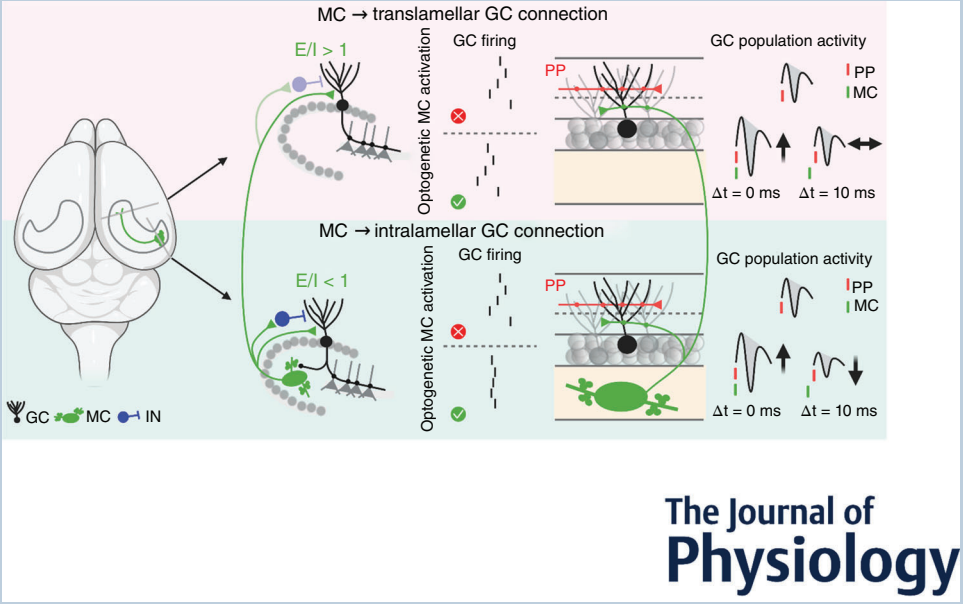

Abstract The hippocampus is an elongated brain structure which runs along a ventral-to-dorsal axis in rodents, corresponding to the anterior-to-posterior axis in humans. A glutamatergic cell type in the dentate gyrus (DG), the mossy cells (MCs), establishes extensive excitatory collateral

Wahab Imam Abdulmajeed obtained his bachelor's and master's degrees in Physiology from the University of Ilorin, Ilorin, Nigeria. Thereafter, he joined the Taiwan International Graduate Program in Interdisciplinary Neuroscience (TIGP–INS). He is currently completing his PhD at National Yang Ming Chiao Tung University, Taipei, Taiwan under the supervision of Prof. Cheng-Chang Lien. His PhD research focuses on understanding hilar mossy cell connectivity and synaptic features along the hippocampal longitudinal axis. His goal is to continue to use multi-level approaches to understand changes in synaptic plasticity and excitation–inhibition balance in health and disease.

DOI: 10.1113/JP282804

connections with the DG principal cells, the granule cells (GCs), and inhibitory interneurons in both hippocampal hemispheres along the longitudinal axis. Although coupling of two physically separated GC populations via long-axis projecting MCs is instrumental for information processing, the connectivity and synaptic features of MCs along the longitudinal axis are poorly defined. Here, using channelrhodopsin-2 assisted circuit mapping, we showed that MC excitation results in a low synaptic excitation–inhibition (E/I) balance in the intralamellar (local) GCs, but a high synaptic E/I balance in the translamellar (distant) ones. In agreement with the differential E/I balance along the ventrodorsal axis, activation of MCs either enhances or suppresses the local GC response to the cortical input, but primarily promotes the distant GC activation. Moreover, activation of MCs enhances the spike timing precision of the local GCs, but not that of the distant ones. Collectively, these findings suggest that MCs differentially regulate the local and distant GC activity through distinct synaptic mechanisms.

(Received 6 April 2022; accepted after revision 1 June 2022; first published online 7 June 2022)
Corresponding author Cheng-Chang Lien, Institute of Neuroscience, National Yang Ming Chiao Tung University, 155, Section 2, Li-Nong Street, Taipei 112, Taiwan. Email: cclien@nycu.edu.tw

Abstract legend figure Hilar mossy cell (MC) pathways differentially innervate dentate granule cells (GCs) and interneurons along the hippocampal longitudinal axis. They mediate a low excitation–inhibition (E/I) balance in intralamellar GCs, but a high E/I balance in translamellar GCs. Notably, optogenetic excitation of MCs enhances the spike timing precision of intralamellar GCs, but not translamellar GCs. Moreover, MC excitation either promotes or suppresses intralamellar GC activity depending on its timing, but primarily promotes translamellar GC activation. Taken together, MCs differentially regulate GC spike timing precision and response to cortical input in a lamella-specific manner.

Key points

- Hippocampal mossy cell (MC) pathways differentially regulate granule cell (GC) activity along the longitudinal axis.
- MCs mediate a low excitation–inhibition balance in intralamellar (local) GCs, but a high excitation–inhibition balance in translamellar (distant) GCs.
- MCs enhance the spiking precision of local GCs, but not distant GCs.
- MCs either promote or suppress local GC activity, but primarily promote distant GC activation.

Introduction

The hippocampus is an elongated structure running from the anterior to posterior pole in humans and from the ventral to dorsal pole in rodents (Fanselow & Dong, 2010; Scharfman, 2007; Scharfman & Myers, 2013; Strange et al., 2014). The dorsal (posterior) part of the hippocampus is associated with spatial navigation and cognitive functions, whereas the ventral (anterior) counterpart has been implicated in mood and motivation (Engen & Anderson, 2018; Femenía et al., 2012; O'Keefe, 1999; Tavares et al., 2015). The hippocampus contains subfields, including the dentate gyrus (DG) and areas CA3, CA2 and CA1. The DG comprises two types of glutamatergic cells – granule cells (GCs) and mossy cells (MCs) – and various types of GABAergic inhibitory interneurons (INs). GCs form 90% of the cells in the DG (Amaral et al., 2007). These cells receive both spatial and non-spatial object information from the cortical regions and relay the information to the downstream CA regions (Diamantaki et al., 2016; GoodSmith et al., 2017; Jeewajee et al., 2008). The trisynaptic DG–CA3–CA1 pathway transfers information along the lamellar axis. In contrast, MCs receive convergent inputs from GCs and give rise to divergent projections along the longitudinal axis. A major hypothesis posits that MCs can synchronize spatially distinct GCs at different levels of the DG, allowing the integration of many active GCs at distant regions (Buckmaster & Schwartzkroin, 1994; Henze & Buzsáki, 2007). Therefore, MCs can transform the two-dimensional DG into a functional three-dimensional unit (Amaral & Witter, 1989).

MCs establish divergent local and commissural connections with GCs and inhibitory INs (Amaral, 1978; Buckmaster et al., 1992, 1996; Hsu et al., 2016; Larimer & Strowbridge, 2008; Milstein & Soltesz, 2017; Scharfman, 1995, 2016). MC excitation of local INs is robust. Therefore, MC activation modulates overall activity of GCs by laterally inhibiting them (Amaral et al., 2007; Ewell & Jones, 2010; Hsu et al., 2016; Lee et al., 2016;

Liu et al., 2014; Scharfman, 1995; Wang et al., 2021; Yeh et al., 2018). We recently demonstrated that MCs project commissurally and exert predominantly inhibitory effects on contralateral GCs by exciting local GABAergic INs under *ex vivo* and *in vivo* conditions (Hsu et al., 2016; Wang et al., 2021). Compared to MC commissural connections, little is known about the function of MC translamellar connections.

When an animal explores a new environment, the novel event or feature can trigger an emotional response. The spatial information and novelty signal are primarily encoded by the dorsal and ventral poles of the hippocampus, respectively. A recent study found that activation of MCs in the ventral hippocampus transmits a teaching signal, thereby reinforcing contextual learning (Fredes & Shigemoto, 2021; Fredes et al., 2021). Although coupling of the ventral and dorsal poles of the hippocampus through intrahippocampal long axis circuitry is essential for novelty-dependent memory enhancement, the connectivity feature and collateral effect on GCs along the long axis produced by the MC translamellar projections remain unclear.

Taking advantage of transgenic mice that express Cre-recombinase in MCs, we aimed to investigate connectivity and synaptic features of the inputs from hilar MCs to GCs of the DG along the hippocampal long axis. Using a combination of electrophysiological and optogenetic approaches, we found that MC excitation results in distinct and opposite synaptic excitation–inhibition (E/I) balance at synapses of local and distant GCs in brain slices. Moreover, we demonstrated that MC longitudinal projections differentially regulate local and distant GC activity in *ex vivo* and *in vivo* conditions.

Methods

Animals

Calcitonin receptor-like receptor (Crlr)-Cre mice (C57BL/6N-Tg(Calcrl,cre)4688Nkza/J) were obtained from Dr Kazu Nakazawa (Jinde et al., 2012). This mouse line allows for Cre-dependent viral labelling of MCs and their axons (Botterill et al., 2021; Butler et al., 2022; Houser et al., 2021; Jinde et al., 2012; Wang et al., 2021). Male and female mice (age, 3–4 months) were used in this study. All mice were bred into the C57BL/6J background. Mice were housed at the National Yang Ming Chiao Tung University under a 12 h light–dark cycle and provided with food and water *ad libitum*. Animals were handled in accordance with the national and institutional guidelines. All experimental protocols (protocol number: 1051235, 1070417) were approved by the Institutional Animal Care and Use Committee of National Yang Ming Chiao Tung University.

Stereotaxic injection

Mice were anaesthetized with 4% (v/v) isoflurane (Halocarbon Laboratories, North Augusta, SC, USA) in a 100% oxygen-containing induction chamber. Subsequently, the mice were fixed in a stereotaxic frame (IVM-3000; Scientifica, Uckfield, UK). The nose of each mouse was covered by an anaesthetizing mask through which isoflurane (approximately 1.5%) was delivered at 4 ml/min. A homeothermic pad (TMP-5b, Supertech Instruments, Budapest, Hungary) was placed below each mouse to maintain the body temperature at approximately 36°C. The mouse's head was secured with ear bars and the surgical area was sterilized using 75% ethanol. Ophthalmic gel was applied to the eyes to prevent dryness and analgesia (ketorolac, 6 mg/kg) was administrated preoperatively. A midline scalp incision (1 cm) was made with scissors and the scalp was pulled aside to expose the skull. The stereotaxic injections were performed as previously described (Hsu et al., 2016; Lee et al., 2016). Briefly, to inject the adeno-associated virus (AAV) into the DG hilus to target MCs, a small craniotomy was made above the ventral DG or dorsal DG relative to the bregma position (ventral DG, mediolateral (ML): 2.8 mm and anteroposterior (AP): −3.5 mm; dorsal DG, ML: 1.2 mm and AP: 1.7 mm). AAV5-EF1α-DIO-hChR2-(H134R)-eYFP (4.3×10^{12} vector genomes/ml, University of North Carolina, Chapel Hill, NC, USA) was injected with a 10-μl NanoFil syringe (World Precision Instruments, Sarasota, FL, USA). A 34-gauge bevelled Nanofil needle loaded with the virus-containing solution was gently lowered to the ventral DG (ML: 2.8 mm, AP: −3.5 mm, and dorsoventral (DV): −2.8 mm) or dorsal DG (ML: 1.2 mm, AP: 1.7 mm and DV: 1.9 mm). A 300-nl volume of the virus-containing solution was injected into the DG at a rate of 0.1 μl/min under the control of a nanopump (KDS-310-PLUS, KD Scientific, Holliston, MA, USA). The needle was left in place for 10 min after injection before it was gently removed at a slower rate. All mice were given at least a 3-week post-surgical recovery period prior to undergoing the electrophysiological experiments. In addition to MCs, CA3 neurons in Crlr-Cre mice express Cre recombinase (Jinde et al., 2012). Therefore, we discarded slices with enhanced yellow fluorescent protein (eYFP) expression in the CA3 area (approximately 10% of total slices) to avoid the possible influence of back-projection of CA3 neurons to the DG (Scharfman, 2007; Swaminathan et al., 2018).

In vivo juxtacellular recording

Mice were anaesthetized with 4% isoflurane during the induction period and placed onto the stereotaxic frame and anaesthetized with 1–1.5% isoflurane in 100% oxygen-containing airflow. The body temperature

was maintained using a heating pad (TMP-5b, Supertech Instruments, Budapest, Hungary). To implant the recording electrode, craniotomies were performed above the dorsal DG (ML: 0.8 to 1.3 mm, AP: −1.5 to −2.0 mm) or ventral DG (ML: 2.4 to 2.8 mm, AP: −3.2 to −3.5 mm). An optical fibre (200 μm diameter) with a ferrule (1.25 mm diameter and 6.4 mm length) was positioned 70° to the surface and placed at the following coordinates for the ventral DG: AP: −3.5 mm; ML, 3.3 mm and DV: 2.0 mm. Activation of channelrhodopsin-2 (ChR2)-expressing MCs was achieved by delivering blue light through a 473-nm laser (OEM Laser Systems, Midvale, UT, USA) with 35 mW light intensity (Wang et al., 2021). For juxtacellular recording, a single-barrel borosilicate capillary glass electrode (outer diameter, 1.2 mm; inner diameter, 0.68 mm; A-M system, Carlsborg, WA, USA) was filled with 1.5–2% Neurobiotin (SP-1120, Vector Laboratories, Burlingame, CA, USA) in 0.5 M NaCl. The pipette impedance was between 5 and 12 MΩ. Juxtacellular labelling was performed by injecting an anodal current pulse (0.5–10.0 nA, 200 ms) as previously described (Pinault, 1996). Signals from the pre-amplification headstage were amplified 1000-fold and high-pass filtered at 1 Hz (ELC01-MX, NPI Electronic, Tamm, Germany). Signals were band-pass filtered at 1–5 kHz and sampled at 40 kHz by a digitizer (Digidata 1440A, Molecular Devices, San Jose, CA, USA). Spikes were band-pass filtered at 300 to 5 kHz during signals acquisition (DPA-2FS, NPI Electronic).

Preparation of brain slices

Mice were sacrificed by rapid decapitation 3–4 weeks after injection of the virus. Acute coronal (90% of experiments) or transverse brain slices of 300 μm thickness were cut using a microslicer (DTK1000, Dosaka, Kyoto, Japan) in an ice-cold sucrose solution containing (in mM) 87 NaCl, 25 $NaHCO_3$, 1.25 NaH_2PO_4, 2.5 KCl, 10 glucose, 75 sucrose, 0.5 $CaCl_2$ and 7 $MgCl_2$. Slices were recovered in an oxygenated (95% O_2–5% CO_2) sucrose solution-containing chamber at 34°C for 30 min and kept at 23 ± 2°C until used.

Patch-clamp recording and optical stimulation

For electrophysiological recordings, slices were individually transferred to the recording chamber and continuously perfused with oxygenated artificial cerebrospinal fluid (ACSF) containing (in mM): 125 NaCl, 25 $NaHCO_3$, 1.25 NaH_2PO_4, 2.5 KCl, 25 glucose, 2 $CaCl_2$ and 1 $MgCl_2$ at 23 ± 2°C. The ChR2-eYFP expression was confirmed by yellow fluorescence and neurons in the DG were visually selected for recordings using a Dodt gradient contrast-based microscope (BX51WI, Olympus, Tokyo, Japan).

Whole-cell patch-clamp recordings were obtained from single cells in voltage- or current-clamp mode. Recording electrodes (4–6 MΩ) were pulled from borosilicate glass with an inner filament (outer diameter, 1.5 mm; inner diameter, 0.86 mm; Harvard Apparatus, Holliston, MA, USA) and filled with a low Cl^- ($[Cl^-]$ = 7.2 mM) internal solution containing (in mM): 136.8 potassium gluconate, 7.2 KCl, 0.2 EGTA, 4 MgATP, 10 HEPES, 7 Na_2-phosphocreatine, 0.5 Na_3GTP (pH 7.3 with KOH), and 0.4% (w/v) biocytin (Thermo Fisher Scientific, Waltham, MA, USA) or a Cs-based Cl^- ($[Cl^-]$ = 35 mM) internal solution containing (in mM): 121.5 $CsMeSO_3$, 13.5 $CsCl_2$, 10 HEPES, 0.1 EGTA, 5 QX-314 bromide, 4 $MgCl_2$, 2 Na_2ATP, 10 Na_2-phosphocreatine, 0.3 Na_3GTP (pH adjusted to 7.3 with CsOH), and 0.4% (w/v) biocytin. The experimentally determined reversal potential with the low Cl^- ($[Cl^-]$ = 7.2 mM) internal solution for $GABA_A$ receptor (E_{GABA}) was ∼75 mV (for experiments in Figs 1*F*, 5, 8 and 9) and with the Cs-based low Cl^- ($[Cl^-]$ = 35 mM) internal solution for $GABA_A$ receptor (E_{GABA}) was ∼−40 mV and for AMPA receptor (E_{AMPA}) was ∼+10 mV (for experiments in Figs 3*C* and *D*, 4*B* and *H*, 6 and 7). In a subset of experiments (Fig. 3*B*, 4*C* and 4*I*), the glass pipettes were filled with a high Cl^- ($[Cl^-]$ = 144 mM) internal solution containing the following (in mM): 140 KCl, 15 potassium gluconate, 0.1 EGTA, 2 $MgCl_2$, 4 Na_2ATP, 10 HEPES, 0.5 Na_3GTP and 0.4% (w/v) biocytin (pH adjusted to 7.3 with KOH or HCl). The experimentally determined reversal potential with this high Cl^- ($[Cl^-]$ = 144 mM) internal solution for the $GABA_A$ receptor (E_{GABA}) was ∼0 mV and for the AMPA receptor (E_{AMPA}) was ∼0 mV.

To measure the excitatory and inhibitory conductance in GCs, a Cs-based intracellular solution was used as aforementioned. Excitatory and inhibitory synaptic responses were evoked by 5-Hz photostimulation of MC terminals in ventral or dorsal GCs (5 ms; ∼3 mW, 470 nm) with a 15 s inter-sweep interval. Excitatory and inhibitory synaptic responses were recorded while holding the cells at −40 and +10 mV, respectively. An unbiased protocol was designed such that both excitatory postsynaptic currents (EPSCs) and inhibitory postsynaptic currents (IPSCs) were recorded in the same sweep/train by automatically switching the holding potential within sweeps (Hsu et al., 2016). An average of 20 sweeps was used to determine the current amplitudes. In a subset of experiments, a high Cl^- internal solution (E_{GABA} = ∼0 mV; E_{AMPA} = ∼0 mV) was used. Light-evoked responses were recorded from GCs, which were held at −70 mV. After obtaining stable responses, 1 μM SR95531 (SR) was applied to block the $GABA_A$-mediated component. Finally, 2 mM of Kyn, a glutamate receptor blocker, was applied to block the remaining current component. The $GABA_A$-mediated component was obtained by digitally subtracting the Kyn-sensitive trace from the baseline trace recorded in the

presence of only ACSF. Only recordings with stable series resistance (<30 MΩ) were considered for further analysis.

In the spike timing precision experiments, a 5-Hz sinusoidal current was delivered when recorded cells were held at −75 mV, near the reversal potential of $GABA_A$ receptors. The injected current (peak to trough, range: 50–150 pA) was adjusted to generate single action potentials near the peak of the sine waveform. Twenty sweeps were recorded with a 15 s inter-sweep interval. Then, we detected synaptic connections by recording the postsynaptic current in the target cells via the application of a 5-Hz photostimulation while holding the cells at −75 mV. Only cells that responded to the photostimulation were used in further experiments. After that, the sinusoidal current injection was paired with 5-Hz square photostimulation of ventral MC in the ventral DG or ventral MC terminals in the dorsal DG for another 20 sweeps. The light stimulation occurred close to the peak (79–97°) of the sinusoidal waveform. To determine the spike jitter and phase, the time of the peak of each spike was converted to the phase angle using customized Python codes. The mean and standard deviation (SD) were used to denote the spike phase (latency) and spike jitter, respectively.

To test the ability of MCs in modulating action potential generation in GCs, we drove GC firing by delivering increments (0–120 pA) of a 5-Hz sinusoidal current and then paired it with a 5-Hz square pulse photostimulation of the MC terminals. Each step of the current injection consisted of five sine waves. The light stimulation was delivered either near (Δt = 1.2 ms, an interval defined from the onset of light pulse to the peak) or preceding (Δt = 28.8 ms) the peak of the sine waveform. We chose these two specific intervals to investigate the effects of excitatory postsynaptic conductance (EPSG) and inhibitory postsynaptic conductance (IPSG) selectively on action potential generation. The fast-spiking phenotype of hippocampal INs or putative soma-targeting INs recorded at room temperature (21–24°C) were defined by their maximal firing rate >65 Hz and coefficient of variation <0.2 in response to a 1 s depolarizing current injection (Ajibola et al., 2021; Lien & Jonas, 2003). Recordings were made with Multiclamp 700B amplifiers (Molecular Devices), low-pass filtered at 4 kHz and digitized at 10 kHz (Digidata 1440A, Molecular Devices), and controlled by pCLAMP 10.3 software (Molecular Devices).

To study the collateral effect of ventral MCs on ventral and dorsal GC activation in response to the medial perforant path (MPP) input, local field potential recordings were made using the glass electrode (tip diameter, ∼5 μm) filled with ACSF. The recording electrode was placed in the ventral or dorsal granule cell layer to monitor the pSpike in response to MPP stimulation. The glass pipette (tip diameter; ∼10 μm containing the stimulation electrode (coated silver wire) filled with ACSF was placed in the middle molecular layer (MML) to stimulate the MPP fibres. To obtain the input–output relationship, variable current pulses (50–250 μA, 0.1 ms) were applied every 30 s using a stimulus isolator (Isoflex, A.M.P.I.). Subsequently, using stimulus that evoked 30–50% of the maximum pSpike, we either paired the electrical stimulation of the medial perforant path with the photostimulation (5 Hz, 10 ms) of ventral MC (vMC) in the ventral DG or vMC terminals in the dorsal DG (Δt = 0 ms), or the photostimulation (5 Hz, 10 ms) of vMC in the ventral DG or vMC terminals in the dorsal DG preceded the medial perforant path stimulation by 10 ms (Δt = −10 ms; Hsu et al., 2016).

In this study, the coronal section was defined as either the dorsal DG or ventral DG according to the mouse atlas (Paxinos & Franklin, 2001). The ventral DG slices corresponded to the AP coordinates ranging from −2.70 to −3.8 mm (relative to the bregma), whereas the dorsal DG slices corresponded to the AP coordinates ranging from −1.22 to −1.80 mm.

Immunohistochemistry

Mice were anaesthetized with isoflurane. Each mouse was perfused transcardially with cold 0.1 M phosphate-buffered saline (PBS), followed by 4% (w/v) paraformaldehyde (PFA) freshly prepared in 0.1 M PBS. Mouse brains were excised and post-fixed in the same solution overnight. Coronal slice sections of 50 μm in thickness containing the hippocampal regions were prepared using a microtome (SM2010R, Leica Microsystems, Wetzlar, Germany). The immunostaining protocol was modified from a previous study (Duffy et al., 2013). Briefly, slices were blocked in 10% normal goat serum (NGS) in 0.1 M PBS containing 0.25% Triton X-100 and 0.005% bovine serum albumin for 1 h at room temperature. The sections were then incubated in one of the following primary antibodies: anti-glutamate receptor 2/3 subunit (GluA2/3; AB1506; 1:100; Millipore, Billerica, MA, USA); anti-green fluorescent protein (AB290; 1:1000; Abcam, Cambridge, MA, USA); anti-somatostatin (SST; T-4103; 1:10000; Peninsula, St Helens, UK); anti-parvalbumin (PV; AB181086; 1:500; Abcam) prepared in 1% NGS and 0.25% Triton X-100 in 0.1 M PBS for 24 h or overnight at 4°C. After primary antibody incubation and three 10 min washes in 0.1 M PBS at room temperature, sections were incubated for 2 h in the secondary antibody (goat anti-rabbit Alexa Fluor 594 or Alexa 488 Fluor 1:400; Thermo Fisher Scientific) at room temperature. All procedures were performed with continuous shaking. For biocytin labelling, each recorded cell was fixed in 4% PFA overnight. After washing out the PFA in 0.1 M PBS for 3 times at room temperature, each slice was incubated in 0.3% (v/v) Triton X-100 (USB Co., Cleveland, OH, USA) in PBS for 30 min and blocked in 10% NGS (Vector

Laboratories) for 2 h at room temperature. Further, each slice was incubated in Alexa Fluor 594 or Alexa Fluor 555 conjugated secondary antibodies prepared in 0.3% PBST containing 1% NGS for 2 h at room temperature or overnight at 4°C. Each slice was washed in 0.1 M PBS six times and mounted onto slides with Vectashield mounting medium (Vector Laboratories) with 4′,6-diamidino-2-phenylindole (DAPI, H-1200, Vector Laboratories). Fluorescently labelled neurons were examined by confocal microscopy using a model SP5 microscope (Leica Microsystems) or LSM 700 microscope (Carl Zeiss, Jena, Germany) using ×20, ×40, or ×63 oil immersion objective lenses. GluA2/3-, PV-, or SST-immunoreactive cells were identified in *z*-stack images and examined for colocalization with ChR2-eYFP-expressing cells. The co-labelled cells were counted using the counter plugin in Fiji (a distribution of ImageJ software, NIH, Bethesda, MD, USA, 1.53c; Ajibola et al., 2021; Schindelin et al., 2012).

Data and statistical analyses

All data were analysed offline using Prism 6.0 (GraphPad Software, La Jolla, CA, USA), Clampfit 10.3 (Molecular Devices) or customized Python codes. The timing of the action potential peak was converted to phase angles (degree) using a customized Python code. The jitter was defined as the SD of the phase angles (degree). To calculate the conductance, the EPSC and IPSC were divided by their respective driving forces. The E/I ratio was calculated by dividing the excitatory conductance by the inhibitory conductance. The synaptic latency was determined as the time elapsed from the light onset to the onset of the synaptic response (Ajibola et al., 2021; Hsu et al., 2016). The onset of the synaptic response was determined by the intersection of a line through the 20% and 80% points of the rising phase of the EPSC or IPSC. Statistical significance was tested using the Mann–Whitney test, Wilcoxon signed-rank test, two-way ANOVA or two-way repeated measures ANOVA followed by the Bonferroni *post hoc* test. Data are shown as means ± SD. *P*-values were indicated in figure legends: $^{*}P < 0.05$, $^{**}P < 0.01$, $^{***}P < 0.001$, $^{****}P < 0.0001$.

Results

Selective expression of ChR2 in MCs and their axonal projections

To investigate the axonal projections of MCs along the hippocampal longitudinal axis, an adeno-associated virus type 5 (AAV5) carrying a light-sensitive ChR2-eYFP was injected unilaterally into the ventral DG of Crlr-Cre mice (Fig. 1*A*). This mouse line was used for Cre-dependent viral labelling of MCs and their axons according to the literature (Botterill et al., 2021; Butler et al., 2022; Houser et al., 2021; Jinde et al., 2012; Wang et al., 2021). Three weeks after the viral injection, ChR2-eYFP expression was detected in the somata and the processes of hilar MCs at the injection site (Fig. 1*B* and *C*, right bottom). ChR2-eYFP-expressing axons were observed bilaterally in the inner molecular layer (IML) along the septotemporal axis (Fig. 1*B*–*D*). Similar results were obtained with injection of AAV5-ChR2-eYFP into the dorsal DG of Crlr-Cre mice, except that the expression of ChR2-eYFP-expressing axons was mostly restricted in the middle molecular layer (MML) in the ventral DG (data not shown). To confirm the specificity of ChR2-eYFP expression, we examined glutamate receptor 2/3 subunit (GluA2/3) expression at the injection site. The majority (96.5 ± 4.6%, 12 slices from 2 mice) of the ChR2-eYFP-expressing cells (177 cells, 12 slices, 2 mice) in the hilus were GluA2/3-immunoreactive cells (Fig. 1*Ea*). This observation is consistent with findings of previous reports showing that MCs, but not hilar INs, of the DG express GluA2/3 (Bui et al., 2018; Duffy et al., 2013; Fujise & Kosaka, 1999; Wang et al., 2021). To confirm that INs were not infected by the virus, we stained for parvalbumin (PV) and somatostatin (SST), which are markers of major INs in the DG. In total, 133 ChR2-eYFP-expressing cells were identified in the hilus (from 7 slices, 2 mice). There was no colocalization between the ChR2-eYFP-expressing cells and PV-expressing cells (36 cells from 7 slices, 2 mice; Fig. 1*Eb*). Similarly, for SST-expressing cells, a total of 65 ChR2-eYFP-expressing cells were identified in the hilus (from 4 slices, 2 mice). There was no colocalization between the ChR2-eYFP-expressing cells and SST-expressing cells (58 cells from 4 slices, 2 mice; Fig. 1*Ec*). These observations are consistent with those of previous studies in which Cre-dependent ChR2-eYFP expression was highly specific to MCs in the Crlr-Cre line in the DG (Bui et al., 2018; Houser et al., 2021; Jinde et al., 2012; Wang et al., 2021). Then, we characterized the response of ChR2-eYFP-expressing MCs in brain slices to light stimulation using the patch-clamp whole-cell recording (Fig. 1*F*). Repetitive blue light pulses (470 nm; 3 mW; 5 ms) at 10 Hz induced recorded cell spiking in the current-clamp mode (Fig. 1*F*, top) and large inward currents in the voltage-clamp mode (Fig. 1*F*, bottom). The cells (5 cells from 3 mice) were filled with biocytin during whole-cell recordings and were *post hoc* morphologically recovered (Fig. 1*G*). Typical thorny excrescences were observed on the proximal dendrites of this representative ChR2-eYFP-expressing MC (Fig. 1*G*, arrowheads). Finally, we performed *in vivo* juxtacellular recordings from MCs in the ventral DG and tested their response to light stimulation (Fig. 1*H*). Similar to slice recordings, the spike activity of a putative MC increased in response to photostimulation (Fig. 1*H*).

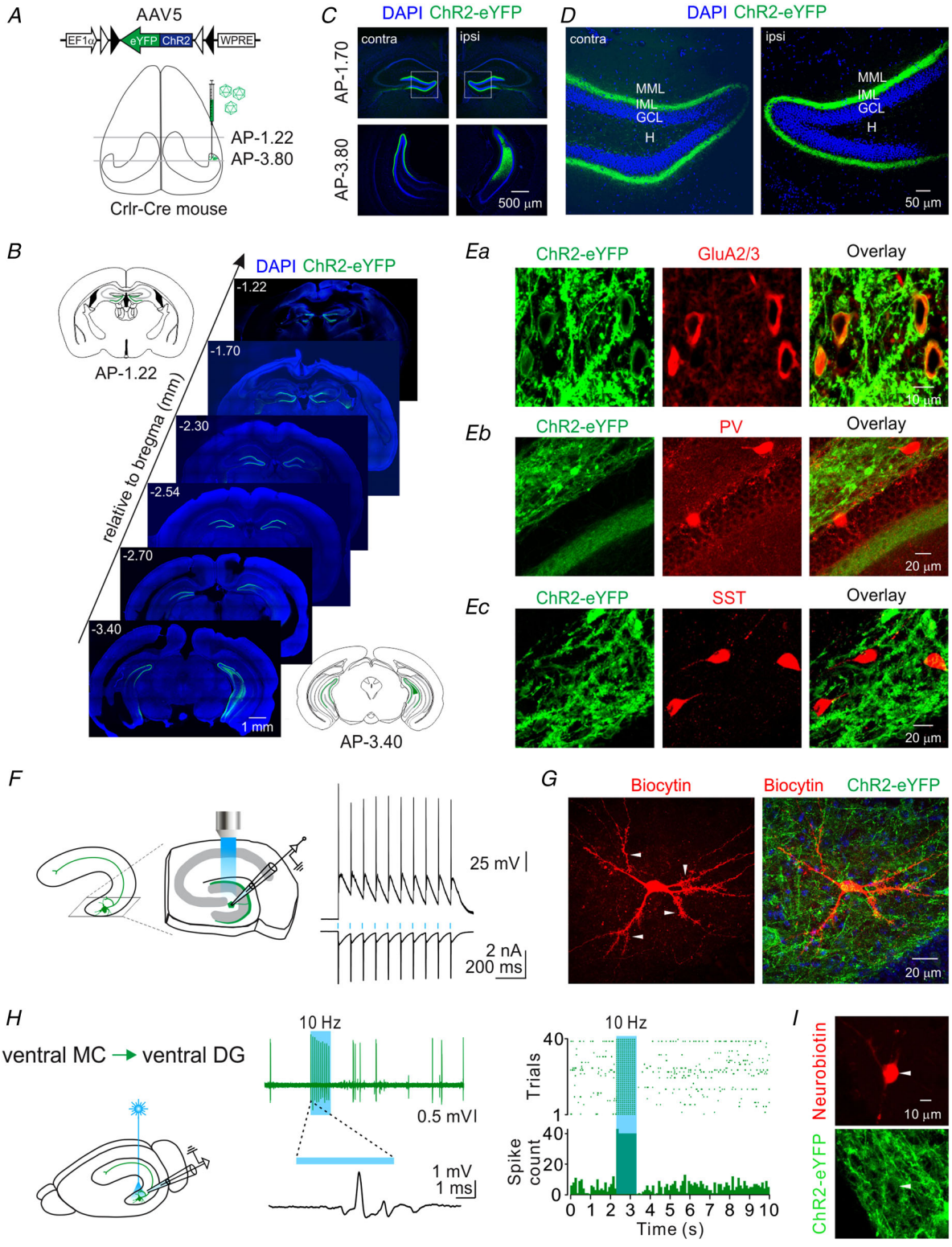

Figure 1. Selective labelling and manipulation of MCs and their axonal projections
A, schematic representation of unilateral injection of AAV5-EF1α-DIO-hChR2-(H134R)-eYFP into the right ventral DG of a Crlr-Cre mouse. Grey lines indicate the location of coronal sections shown in *C*. *B*, representative coronal sections showing expression of ChR2-eYFP along the ventrodorsal axis of the hippocampus in a Crlr-Cre mouse unilaterally injected with a Cre-dependent virus in the right ventral DG. *C*, representative sections of the dorsal DG (top) and ventral DG (bottom). ChR2-eYFP expression was restricted to the hilus and the IML of the right

ventral DG (virus injection site; bottom right). Moreover, MC terminals were seen at the IML of the contralateral DG (bottom left) as well as the ipsilateral and contralateral dorsal DG (top, right and left). Boxes indicate the enlarged areas shown in *D*. *D*, enlargement of the dorsal DG shown in *C*. The right and left images represent the ipsilateral and contralateral dorsal DG, respectively. The MC axonal projections were restricted to the IML. *Ea*, left to right, high magnification of the hilus from the AAV injection site (right ventral DG) of a Crlr-Cre mouse showing ChR2-eYFP-expressing neurons, GluA2/3 positive cells, and the overlay image which shows that ChR2-eYFP-expressing neurons are GluA2/3 positive cells. *Eb*, left to right, confocal images of the DG from the AAV injection site (right ventral DG) of a Crlr-Cre mouse showing ChR2-eYFP-expressing neurons, PV-expressing INs, and the overlay image which shows no colocalization. *Ec*, left to right, confocal images of the hilus from the AAV injection site (right ventral DG) of a Crlr-Cre mouse showing ChR2-eYFP-expressing neurons, SST-expressing INs, and the merged image which shows no colocalization. *F*, left, experimental schematic representation of photostimulation and recording of a ChR2-eYFP-expressing MC in the hilus of the right ventral DG. The ventral DG was sectioned in the horizontal plane. Right, light-evoked spikes recorded from a ChR2-eYFP-expressing MC at −60 mV in current clamp (top) and action potential-mediated currents and ChR2-mediated photocurrents recorded at −60 mV in voltage clamp (bottom) in response to 10-Hz light pulses (blue bars). *G*, left, the morphology of a biocytin-filled MC. The light-evoked responses are shown in *F*. Arrowheads indicate thorny excrescences. Right, a merged confocal image of ChR2-eYFP and biocytin signals. *H*, left, experimental schematic representation. Juxtacellular recording of an MC from the ventral DG. Left, light stimulation was delivered through an optical fibre, which was inserted into the ventral DG. Middle, a representative trace and the enlargement of a light-evoked spike. Right, the raster plot of spikes from 40 representative sweeps and peristimulus time histogram (PTSH) from all sweeps of a recorded MC. *I*, top, the *post hoc* Neurobiotin-labelled MC (arrowhead) recorded in *H*. Bottom, the expression pattern of ChR2-eYFP. AAV5, adeno-associated virus type 5; DAPI, 4′,6-diamidino-2-phenylindole; DG, dentate gyrus; GCL, granule cell layer; H, hilus; IML, inner molecular layer; INs, inhibitory interneurons; MCs, mossy cells; MML, middle molecular layer; PV, parvalbumin; SST, somatostatin.

After recording, the recorded cell was juxtacellularly labelled with Neurobiotin. The Neurobiotin-filled cell was ChR2-eYFP-positive (Fig. 1*I*). Taken together, these data indicate that ChR2-eYFP-expressing MCs can be activated by photostimulation.

Effects of MC activation on local and distant DG cells

Next, we tested the collateral effect of ChR2-eYFP-expressing MCs in the ventral hippocampus on neurons in the ventral and dorsal DG in response to photostimulation. We performed *in vivo* juxtacellular recordings of DG cells in anaesthetized mice (Fig. 2*A* and *D*). Photostimulation of the MC somata in the ventral DG inhibited a putative GC (spike half-width, ∼0.45 ms; Fig. 2*B*) and activated a morphologically identified IN in the ventral DG (Fig. 2*C*). In contrast, photostimulation of ventral MCs in the ventral DG activated neurons in the ipsilateral dorsal DG (Fig. 2*E* and *F*). In total, there were six responsive cells and one non-responsive cell. After recordings, we performed juxtacellular labelling with Neurobiotin (Pinault, 1996). These six Neurobiotin-filled responsive cells were morphologically identified as either the GC (1 cell; Fig. 2*E*) or INs (5 cells; Fig. 2*F*). Collectively, these findings suggest that ventral GCs and dorsal GCs differentially respond to ventral MC activation *in vivo*.

MCs mediate monosynaptic excitation and disynaptic inhibition in GCs

In vivo data suggest that ventral MCs could have a differential effect on ventral (local) GCs and dorsal (distant) GCs. We then studied the underlying synaptic mechanisms using the ChR2-assisted circuit mapping approach. First, to study the basic wiring properties of MC connection with GCs, we recorded excitatory postsynaptic currents (EPSCs) and inhibitory postsynaptic currents (IPSCs) in response to MC activation from local GCs within the same lamellae at the level of AAV transfection (Fig. 3*A*). Postsynaptic responses to the photostimulation were recorded in the voltage-clamp mode at −70 mV, using a high chloride (Cl^-) internal solution ($[Cl^-]_i$ = 144 mM; E_{GABA} = ∼0 mV; E_{AMPA} = ∼0 mV). As shown in Fig. 3*B* (left traces), the light-evoked inward current consisted of inhibitory and excitatory components, as it was partially blocked by the bath-applied $GABA_A$ receptor antagonist SR95531 (SR; 1 μM) and was completely blocked after the subsequent addition of the ionotropic glutamate receptor blocker kynurenic acid (Kyn; 2 mM). In another subset of experiments (Fig. 3*B*, right traces), Kyn (2 mM) completely inhibited the light-evoked inward current, suggesting monosynaptic glutamatergic transmission and disynaptic GABAergic transmission to GCs. Another experiment was performed using a caesium (Cs)-based internal solution ($[Cl^-]_i$ = 35 mM; E_{GABA} = ∼−40 mV; E_{AMPA} = ∼+10 mV, Fig. 3*C*; see Methods for details), in which EPSCs and IPSCs were recorded at −40 and +10 mV, respectively (Fig. 3*D*). In response to 5-Hz photostimulation, EPSCs and IPSCs exhibited short-term depression. The enlarged first EPSC and IPSC demonstrated that the EPSC preceded the IPSC by ∼4 ms (Δt = 4.1 ± 0.7 ms; n = 5 cells from 2 mice). The synaptic latencies of EPSC and IPSC were 3.3 ± 0.4 and 7.4 ± 0.8 ms (n = 5 cells from 2 mice), respectively

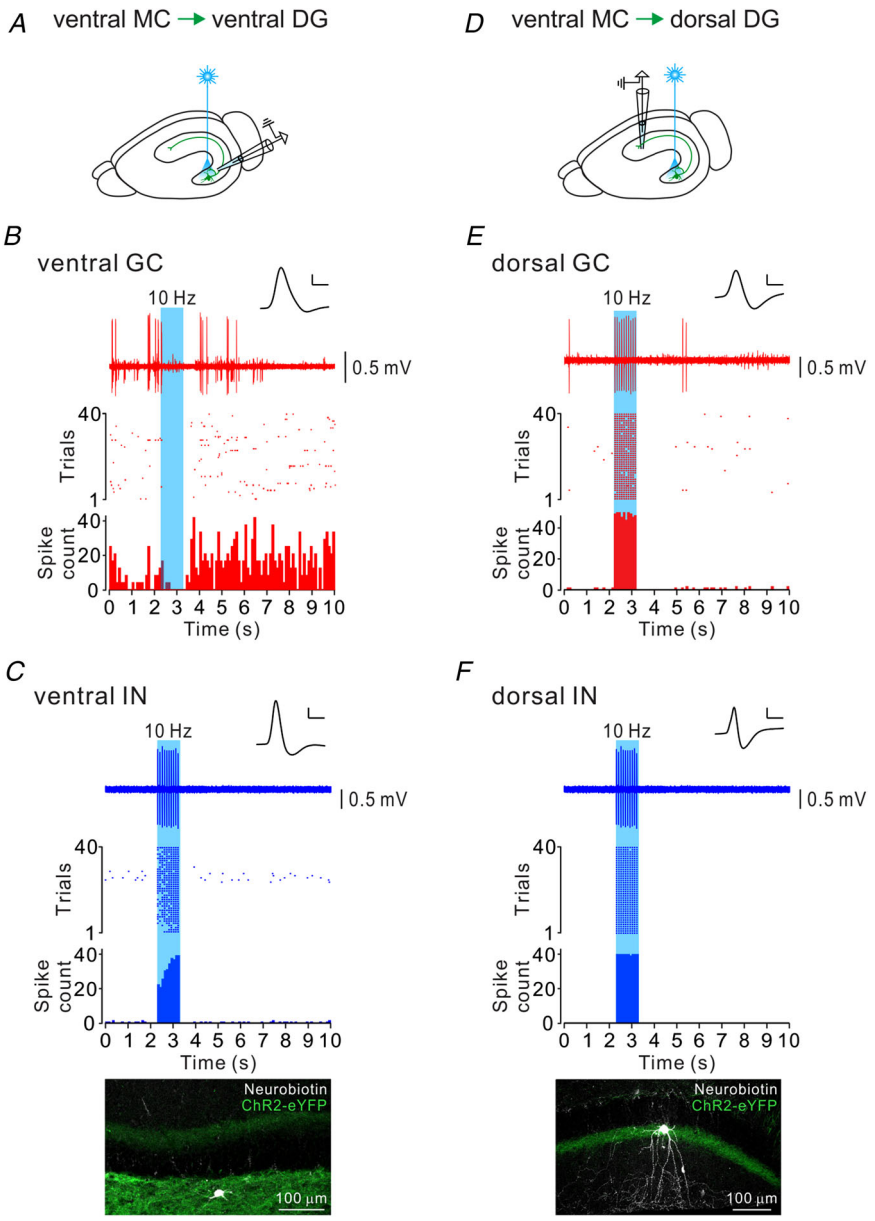

Figure 2. *In vivo* effects of ventral MC activation on GCs and INs in the ventral and dorsal DG
A, experimental schematic representation. Juxtacellular recordings were performed from ventral DG cells during the photostimulation of ventral MCs. *B*, juxtacellular recording of a putative GC (spike half-width, 0.42 ms) from the ventral DG. Top, a representative trace (scale bar, 0.5 mV) and an enlarged spike (scale bars, 0.5 mV/0.5 ms). Middle and bottom, raster plot from 40 representative sweeps and a PSTH from all sweeps of a recorded GC during 10-Hz photostimulation (blue bar). *C*, similar to *B*, juxtacellular recording of an IN (spike half-width, 0.25 ms) from the ventral DG. Top, a representative trace (scale bar, 0.5 mV) and an enlarged spike (scale bars, 0.5 mV/0.5 ms), raster plot and PSTH of a recorded IN during 10-Hz photostimulation (blue bar). Bottom, a Neurobiotin-filled cell (white) with ChR2-eYFP signals (green) in the ventral DG. *D*, experimental schematic representation. Juxtacellular recordings were performed from dorsal DG cells during photostimulation of ventral MCs. *E*, similar to *B*, juxtacellular recording of a biocytin-filled GC (spike half-width, 0.34 ms) from the dorsal DG. Top, a representative trace (scale bar, 0.5 mV) and an enlarged spike (scale bars, 0.5 mV/0.5 ms), raster plot from 40 representative sweeps and a PSTH from all sweeps during 10-Hz photostimulation (blue bar). *F*, juxtacellular recording of an IN (spike half-width, 0.18 ms) from the dorsal DG. Top, a representative trace (scale bar, 0.5 mV) and an enlarged spike (scale bars, 0.5 mV/0.5 ms), raster plot from 40 representative sweeps and a PSTH from all sweeps during 10-Hz photostimulation (blue bar). Bottom, overlay of Neurobiotin-filled cells (white), ChR2-eYFP signals (green) of the recorded IN. DG, dentate gyrus; GC, granule cell; IN, interneuron; MC, mossy cell.

(Fig. 3*E*). Similar results were obtained from dorsal DG slices (Table 1). This is consistent with the notion that GCs, irrespective of their locations, receive monosynaptic excitatory and feedforward inhibitory inputs from MCs (Hashimotodani et al., 2017; Hsu et al., 2016; Wang et al., 2021).

MCs mediate a low E/I ratio in local GCs and a high E/I ratio in distant GCs

We studied E/I balance in ventral and dorsal GCs in response to the photostimulation of MCs along the hippocampal long axis. In this set of experiments, ventral MCs were expressed with ChR2 (Fig. 4*A*). Then, we recorded the EPSCs and IPSCs in GCs using a Cs-based ($[Cl^-]_i$ = 35 mM; E_{GABA} = ∼−40 mV) internal solution at −40 mV and 10 mV, respectively, in response to a 5-Hz light stimulation of the MCs (n = 8 cells from 6 mice). EPSCs and IPSCs depressed substantially in response to the 5-Hz stimulation (Fig. 4*B*). Similarly, using a high Cl^- ($[Cl^-]_i$ = 144 mM; E_{GABA} = ∼0 mV) internal solution (n = 3 cells from 3 mice; Fig. 4*C*), we recorded a mixed excitatory and inhibitory responses from ventral GCs (Fig. 4*C*, black traces). After the bath application of the $GABA_A$ receptor blocker SR (1 μM), the slow GABAergic (SR-sensitive) component was blocked, leaving the fast component (Fig. 4*C*, red traces), which was completely blocked by the subsequent addition of Kyn (2 mM) to the bath solution. The SR-sensitive traces (Fig. 4*C*, blue traces) were obtained by digitally subtracting the Kyn-sensitive (EPSC) component from the baseline (mixed) response. The IPSG was significantly higher than the EPSG (n = 11 cells from 9 mice; Fig. 4*D*; also see Table 1). The plot of each light-evoked response, which consisted of excitatory and inhibitory conductance, demonstrated a clear deviation to the right of the identity

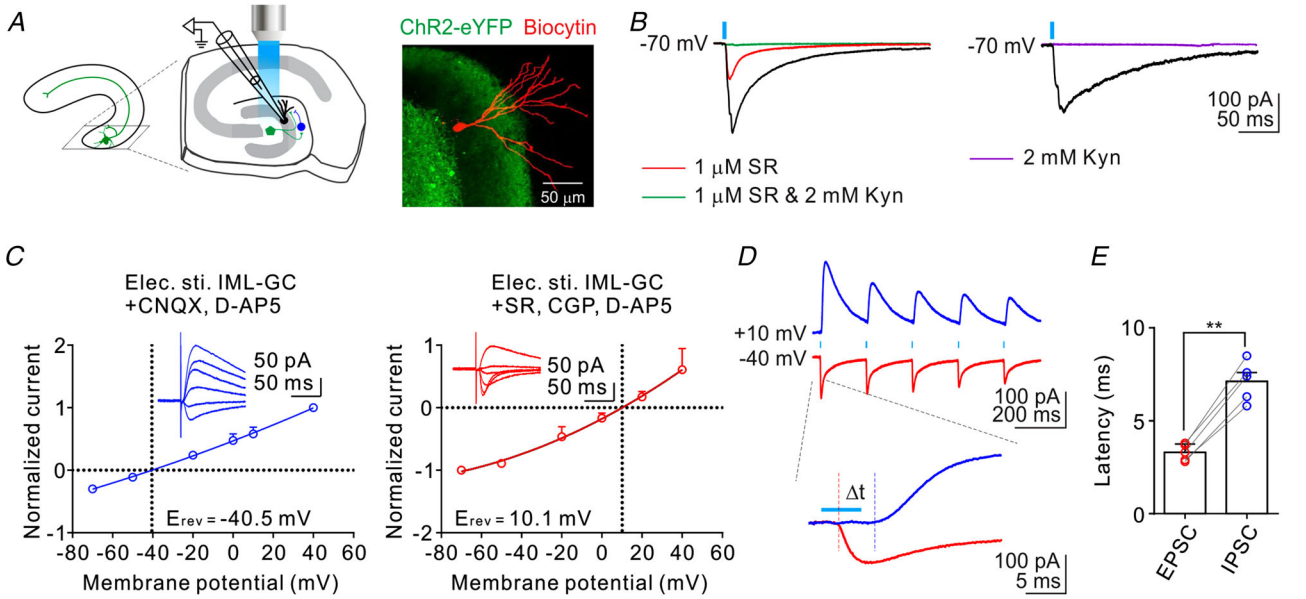

Figure 3. MC activation induces direct excitation and indirect inhibition in GCs
A, left, experimental schematic representation showing the whole-cell patch-clamp recording performed from a GC during photostimulation of ventral MCs. Right, morphology of a biocytin-filled GC (red). *B*, left, light-evoked responses recorded in a GC at −70 mV in voltage-clamp in ACSF (black), in the presence of the $GABA_A$ receptor antagonist SR95531 (1 μM SR; red) and under the subsequent addition of the glutamate receptor blocker kynurenic acid (1 μM SR + 2 mM Kyn; green). Right, light-evoked responses recorded in a GC at −70 mV in ACSF (black) and then in the presence of 2 mM Kyn (purple). *C*, left, representative traces of the IPSC recorded at different holding potentials. Stimulation electrodes were placed in the IML. Plot of the normalized evoked currents against the holding potentials. Data (pooled from 5 cells) fit with a polynomial function. Right, representative traces of the EPSC recorded at different holding potentials. Plot of the normalized evoked currents against the holding potentials. Data (pooled from 3 cells) fit with a polynomial function. *D*, top, sample traces of the EPSC (red; V_{hold} = −40 mV) and IPSC (blue; V_{hold} = +10 mV) recorded in a GC evoked by 5-Hz photostimulation of MCs. Bottom, enlargement of the first response from the top traces revealing the latencies of the EPSC and IPSC. The vertical red and blue dashed lines mark the onset of the EPSC and IPSC, respectively. Δt is the time interval between the onset of the EPSC and IPSC. *E*, a summary of the latencies relative to the light-pulse onset. EPSC latencies were significantly shorter than IPSC latencies; n = 5 cells from 2 mice (Mann–Whitney test; P = 0.0079, U = 0). Error bars indicate SD. ACSF, artificial cerebrospinal fluid; DG, dentate gyrus; EPSC, excitatory postsynaptic current; E_{rev}, reversal potential; GC, granule cell; IML, inner molecular layer; IPSC, inhibitory postsynaptic current; MC, mossy cell.

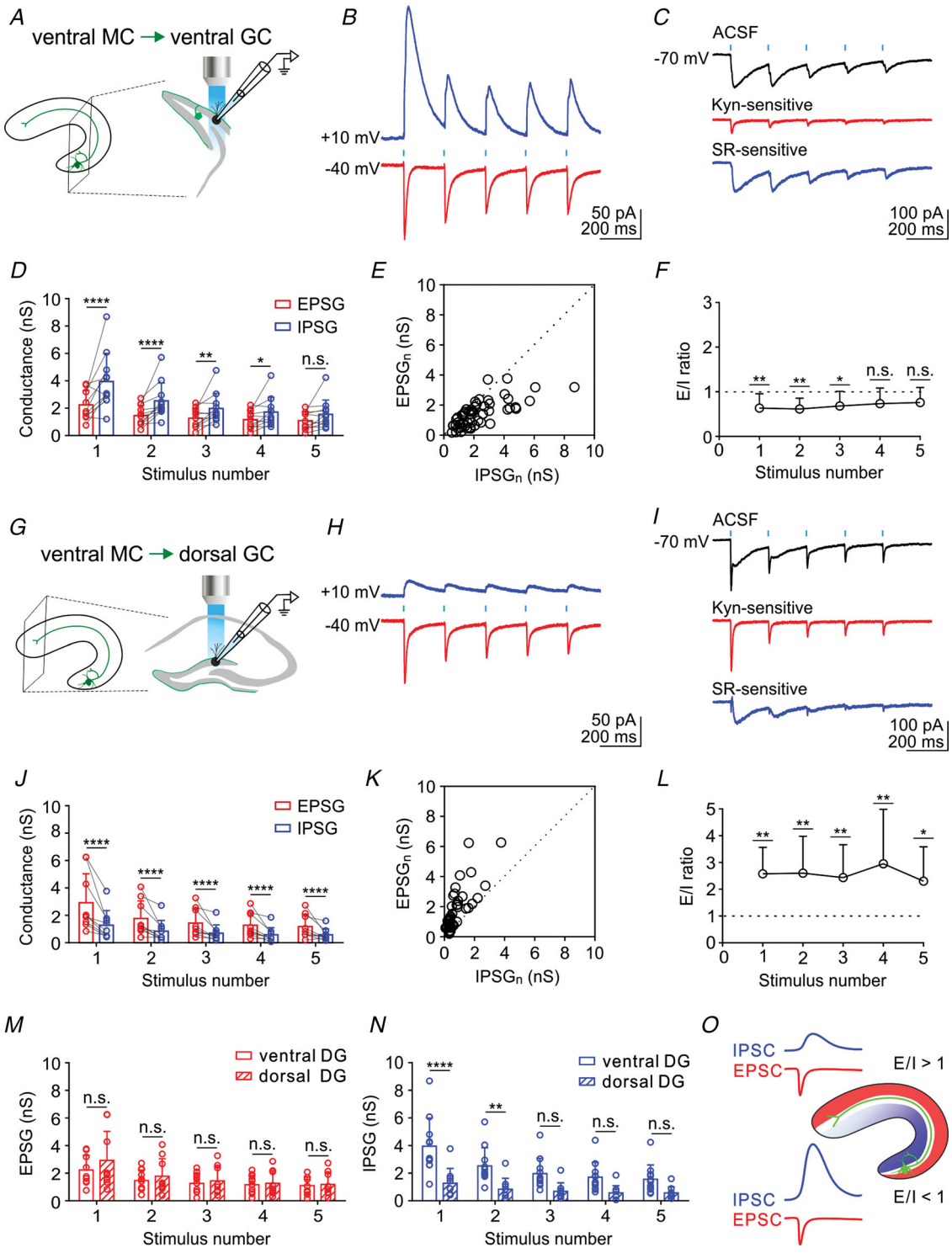

Figure 4. Activating ventral MCs induces a low E/I balance in ventral GCs and a high E/I balance in dorsal GCs

A, experimental schematic representation of whole-cell voltage-clamp recording from a local (ventral) GC. *B*, averaged traces of EPSC (red; $V_{hold} = -40$ mV) and IPSC (blue; $V_{hold} = +10$ mV) of a ventral GC in response to 5-Hz photostimulation of ventral MCs. *C*, top to bottom, traces of light-evoked responses recorded from a ventral GC using a high Cl^- internal solution and holding the cell at −70 mV in voltage-clamp in ACSF (black), in the presence of the $GABA_A$ receptor antagonist SR95531 (1 μM; Kyn-sensitive EPSC, red), and the SR-sensitive component (IPSC, blue) obtained by digitally subtracting the Kyn-sensitive traces from the baseline traces recorded in the

presence of ACSF only. *D*, summary plot of EPSGs and IPSGs of ventral GCs in response to 5-Hz photostimulation of ventral MCs; $n = 11$ cells from 9 mice (two-way repeated measures ANOVA with the Bonferroni *post hoc* test; $P < 0.0001$ for stimulus nos 1 and 2, respectively; $P = 0.0035$, $P = 0.0342$ and $P = 0.1128$ for stimulus nos 3–5, respectively). *E*, distribution of EPSGs and IPSGs of ventral GCs in response to 5-Hz photostimulation of ventral MCs; $n = 55$ from 11 cells and 9 mice. *F*, summary plot of the E/I ratio *versus* the stimulus number of ventral GCs in response to 5-Hz photostimulation of ventral MCs; $n = 11$ cells from 9 mice (Wilcoxon signed-rank test against 1; $P = 0.0098$, $P = 0.0010$, $P = 0.0186$ for stimulus nos 1–3, respectively, and $P = 0.0537$ for stimulus nos 4 and 5, respectively). *G*, experimental schematic representation of whole-cell voltage-clamp recording from a dorsal GC. *H*, averaged traces of EPSC (red; $V_{hold} = -40$ mV) and IPSC (blue; $V_{hold} = +10$ mV) of a dorsal GC in response to 5-Hz photostimulation of ventral MC terminals. *I*, top to bottom, traces of light-evoked responses recorded from a dorsal GC using a high Cl^- internal solution and holding the cell at −70 mV in voltage-clamp in ACSF (black), in the presence of the $GABA_A$ receptor antagonist SR95531 (1 μM; Kyn-sensitive EPSC; red), and the SR-sensitive component (IPSC; blue) obtained by digitally subtracting the Kyn-sensitive traces from the traces recorded in the presence of ACSF only. *J*, summary plot of EPSGs and IPSGs of dorsal GCs in response to 5-Hz photostimulation of ventral MC terminals; $n = 9$ cells from 7 mice (two-way repeated measures ANOVA with the Bonferroni *post hoc* test; all $P < 0.0001$). *K*, distribution of EPSGs and IPSGs of dorsal GCs in response to 5-Hz photostimulation of ventral MC terminals; $n = 45$ from 9 cells and 7 mice. *L*, summary plot of the E/I ratio *versus* the stimulus number of dorsal GCs in response to 5-Hz photostimulation of MC terminals; $n = 9$ cells from 7 mice (Wilcoxon signed-rank test against 1; $P = 0.0039$, $P = 0.0078$, $P = 0.0039$, $P = 0.0078$ and $P = 0.0195$ for stimulus nos 1–5, respectively). *M*, summary of the ventral MC → ventral DG ($n = 11$ from 9 mice) and ventral MC → dorsal DG ($n = 9$ from 7 mice) pathway-mediated EPSGs in GCs (two-way ANOVA with the Bonferroni *post hoc* test; $P = 0.7356$ for stimulus no. 1 and $P > 0.9999$ for stimuli nos 2–5). *N*, summary of ventral MC → ventral DG and ventral MC → dorsal DG pathway-mediated IPSGs in GCs (two-way ANOVA with the Bonferroni *post hoc* test; $P < 0.0001$, $P = 0.0063$, $P = 0.0681$, $P = 0.1324$ and $P = 0.2771$ for stimulus nos 1–5, respectively). *O*, schematic representation showing that in ventral MC → dorsal DG pathway, the excitatory response (EPSG) is similar between the ventral GCs and dorsal GCs while the inhibitory response (IPSG) is larger at the ventral MC → ventral GC synapses. Error bars indicate the SD. See also Table 1. ACSF, artificial cerebrospinal fluid; DG, dentate gyrus; EPSC, excitatory postsynaptic current; EPSG, excitatory postsynaptic conductance; GC, granule cell; IPSC, inhibitory postsynaptic current; IPSG, inhibitory postsynaptic conductance; MC, mossy cell.

line ($n = 55$ from 11 cells, 9 mice; Fig. 4*E*). Consistently, the E/I ratio of each response to the 5-Hz stimulation was approximately 0.6 ($n = 11$ cells, 9 mice; Fig. 4*F*). Similar results were observed in transverse slice sections (data not shown), indicating that MC activation evoked higher inhibition than excitation in local GCs.

We performed similar experiments on GCs located in the dorsal DG using a Cs-based ($[Cl^-]_i = 35$ mM; $E_{GABA} = \sim -40$ mV) internal solution at −40 and 10 mV ($n = 7$ cells from 5 mice; Fig. 4*G*). Interestingly, the EPSC was much larger than the IPSC in dorsal GCs (Fig. 4*H*). Additionally, using a high Cl^- ($[Cl^-]_I = 144$ mM; $E_{GABA} = \sim 0$ mV) internal solution ($n = 2$ cells from 2 mice; Fig. 4*I*), in contrast to our observation in ventral GCs, bath application of SR (1 μM) only blocked the small component of the mixed response in dorsal GCs. The remaining fast component (red traces) was completely blocked by the subsequent addition of Kyn (2 mM) to the bath solution. We observed that the amplitude of SR-sensitive traces (Fig. 4*I*, blue traces) was smaller than the Kyn-sensitive (EPSC, red traces) amplitude. Similarly, the EPSG was significantly greater than the IPSG during successive stimulations ($n = 9$ cells, 7 mice; Fig. 4*J*; Table 1). The plot of light-evoked responses revealed a clear deviation to the left of the identity line ($n = 45$ from 9 cells, 7 mice; Fig. 4*K*), indicating that MC activation evoked higher excitation than inhibition in dorsal GCs. Furthermore, the E/I ratios were >1 during the 5-Hz train stimulation (Fig. 4*L*). This result was not affected by the intensity of light stimulation, sex, cutting plane, and recording temperature (data not shown). Finally, we compared the EPSGs and IPSGs of ventral MC connections along the longitudinal axis. For ventral MC axon projections, equivalent EPSGs were detected from intralamellar (ventral GC; $n = 11$ from 9 mice) and translamellar (dorsal GC; $n = 9$ from 7 mice) GCs (Fig. 4*M* and *O*). In contrast, the IPSGs recorded from the GCs in the dorsal DG were significantly smaller than those in the ventral DG (Fig. 4*N* and *O*). These data indicate that the higher inhibitory conductance might underlie the low E/I ratio recorded at the ventral MC → local GC connection.

Intralamellar INs receive stronger MC excitatory transmission than translamellar INs

MC activation generates disynaptic inhibition in GCs, suggesting direct recruitment of local-circuit INs within the DG lamella. To identify these IN subtypes activated by MCs, we performed patch-clamp recordings from a local IN and an adjacent GC in each brain slice (Fig. 5*A* and *B*). In this set of experiments, only a small number of ventral MCs were expressed with ChR2. INs were randomly selected from the ML, hilus or the border of the granule cell layer–hilus. The simultaneous recordings of an IN and a GC allowed us to normalize ChR2 expression levels

Table 1. Properties of ventral MC → ventral GC and ventral MC → dorsal GC synapses

	Ventral GC (n = 11)	Dorsal GC (n = 9)	P
EPSC (pA)	125.1 ± 22.2	148.3 ± 32.4	0.75
IPSC (pA)	217.8 ± 37.6	69.7 ± 22.7	<0.05
Q_{EPSC} (pC)[a]	2.0 ± 0.4	2.1 ± 0.7	0.68
Q_{IPSC} (pC)[a]	12.8 ± 2.8	3.9 ± 1.7	<0.05
EPSG (nS)[b]	2.2 ± 0.4	2.4 ± 0.6	0.59
IPSG (nS)[b]	3.9 ± 0.7	1.3 ± 0.4	<0.05
EPSC			
Latency (ms)	3.0 ± 0.2	3.2 ± 0.2	0.61
A_f (pA)	92.2 ± 22.7	114.0 ± 21.7	0.39
A_s (pA)	27.6 ± 9.7	27.1 ± 12.5	0.97
τ_f (ms)	7.2 ± 0.5	6.7 ± 0.6	0.65
τ_s (ms)	68.6 ± 8.8	54.3 ± 7.0	0.70
EPSC τ_w (ms)	14.7 ± 1.3	14.0 ± 1.7	0.48
IPSC			
Latency (ms)	7.3 ± 0.6	7.5 ± 0.7	0.84
A_f (pA)	20.2 ± 11.6	16.9 ± 4.0	<0.05
A_s (pA)	237.4 ± 42.1	62.3 ± 24.6	<0.05
τ_f (ms)	15.3 ± 3.2	12.7 ± 4.2	0.80
τ_s (ms)	62.9 ± 0.4	73.7 ± 12.5	0.61
IPSC τ_w (ms)	57.4 ± 4.5	49.2 ± 5.2	0.19
E/I ratio	0.6 ± 0.1	2.3 ± 0.3	<0.05

Three ventral GCs and three dorsal GCs were recorded using the high-Cl^- internal solution; others were recorded using the Cs-based low-Cl^- internal solution. Data were obtained in the whole-cell voltage-clamp configuration at ∼23°C. Mann–Whitney test was performed to compare the means between groups. Values in parentheses indicate the total number of cells for each group.
[a]The charge transfer (Q) was measured as integral area under the postsynaptic currents.
[b]The excitatory or inhibitory conductance (EPSG or IPSG) was calculated by dividing the EPSC amplitude or IPSC amplitude by the respective driving forces.
[c]The E/I ratio was calculated from the EPSG and IPSG.
Abbreviations: A, amplitude; f, fast; s, slow; tau, decay time constant; w, weighted.

and compare the data across slices. Most importantly, this approach enabled the direct comparison of synaptic input strength to INs and GCs in the same slices, while activating an identical group of axons (Hsu et al., 2016; Lee et al. 2013). We measured the amplitudes of the light-evoked EPSCs ($V_{hold} = -75$ mV near the IPSC reversal potential; $[Cl^-]_i = 7.2$ mM; $E_{GABA} = \sim -75$ mV) and converted them to EPSGs. Upon photostimulation, the synaptic responses in INs and GCs revealed single events with a short delay (Fig. 5*C*, bottom traces). Based on target selectivity of their axons and firing patterns (Freund & Buzsáki 1996; Hosp et al., 2014; Hsu et al., 2016; Liu et al., 2014), two major IN populations, i.e. dendrite-targeting INs (D-INs) and soma-targeting (S-INs), were identified in the DG (Fig. 5*C*). Overall, 13 of 18 putative D-INs, which exhibited non-fast spiking and 2 of 5 putative S-INs, which showed fast-spiking patterns, were morphologically confirmed. Compared to GCs, both IN populations in the ventral DG were subjected to higher excitatory transmission by ventral MCs (Fig. 5*D*).

Next, we measured synaptic connections between ventral MCs and INs in the dorsal DG (Fig. 5*E*). The same recordings were made from D-INs, S-INs and GCs in the dorsal DG slices (Fig. 5*F*). Interestingly, EPSCs recorded from D-INs were comparable to those recorded from GCs (Fig. 5*G*, top). Moreover, EPSCs recorded from S-INs were slightly smaller than those recorded from GCs (Fig. 5*G* and *H*, bottom; $P = 0.056$). Overall, INs in the ventral DG were more subject to excitatory transmission by ventral MCs than those in the dorsal DG (Fig. 5*H*; Table 2). Overall, 10 of 12 putative D-INs, which exhibited non-fast spiking, and 3 of 5 putative S-INs, which exhibited fast-spiking patterns, were morphologically confirmed. These findings suggest that a reduced ventral MC excitatory drive to dorsal INs may account for reduced disynaptic inhibition in the dorsal DG.

Dorsal MCs mediate a low E/I ratio in local GCs and a high E/I ratio in distant GCs

Previous studies have demonstrated that several properties of MCs in the dorsal DG differ from those of MCs in the ventral DG (Botterill et al., 2021; Fujise

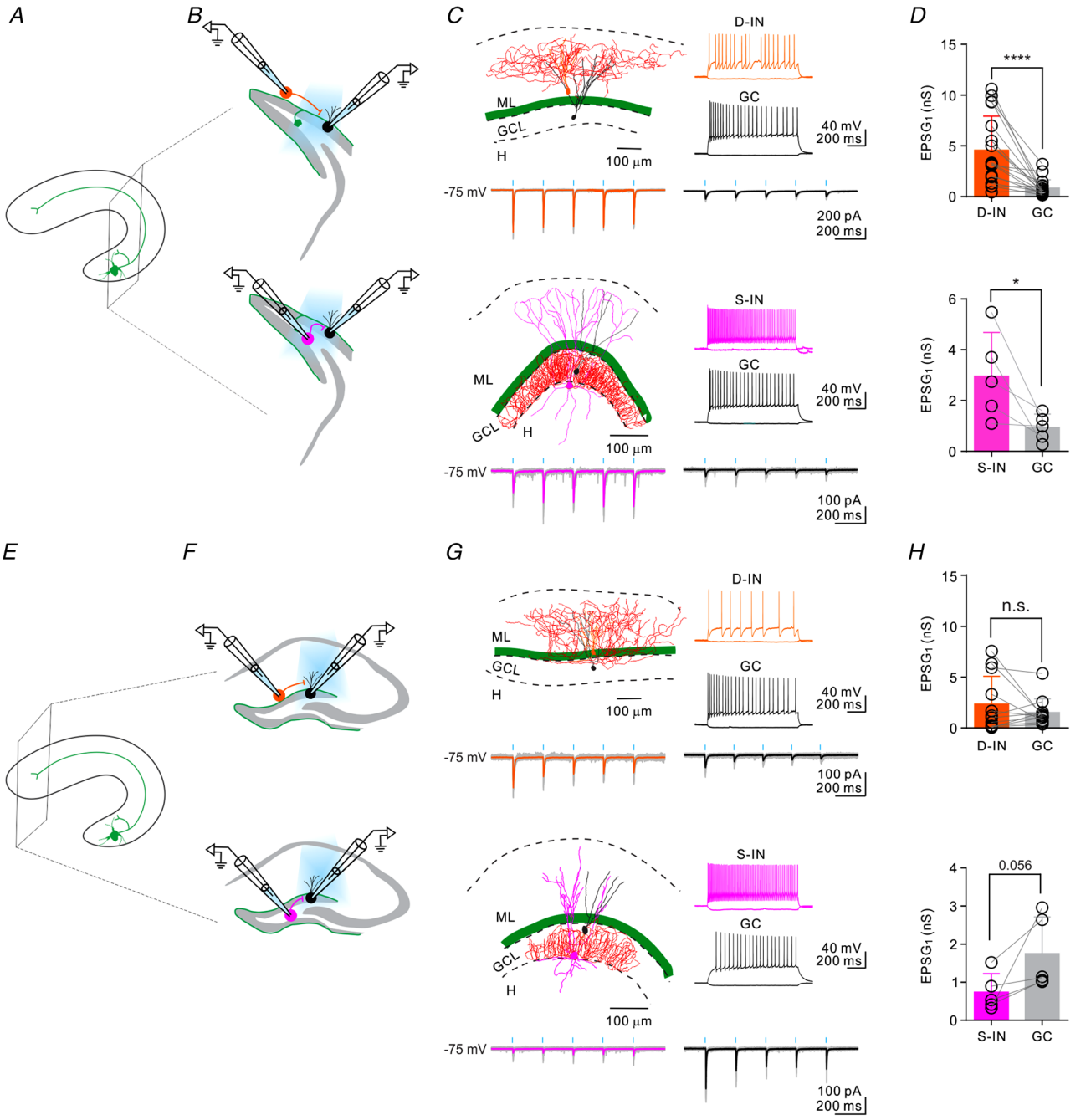

Figure 5. GABAergic INs in the ventral DG and dorsal DG are subject to different excitatory transmissions by ventral MCs

A, schematic representation of a cutting plane through the ventral DG. *B*, schematic representation of dual recordings from a D-IN (orange, top) and a GC (black) or a S-IN (magenta, bottom) and a GC (black) in the ventral DG upon photostimulation of ventral MCs. *C*, top, representative morphological reconstruction of a recorded D-IN (axons in red; soma and dendrites in orange) and a GC (black) and their respective firing patterns. The averaged EPSC traces of the D-IN (orange) and GC (black) are shown. Bottom, representative morphological reconstruction of the recorded S-IN (axons in red; soma and dendrites in magenta) and GC (black) and their respective firing patterns. The averaged EPSC traces of the S-IN (magenta) and GC (black) obtained from the ventral DG are shown. Green areas represent the axonal expression of ChR2-eYFP in the IML. *D*, summary of ventral MC → ventral DG mediated $EPSG_1$ in D-INs and GCs (top) and S-INs and GCs (bottom). The connected lines represent the neurons obtained from the same slice. For D-INs and GCs, $n = 18$ cells from 12 mice (Mann–Whitney test; $P < 0.0001$; $U = 32.50$). For S-INs and GCs, $n = 5$ cells from 5 mice (Mann–Whitney test; $P = 0.0317$; $U = 2.00$). *E*, schematic representation of a cutting plane through the dorsal DG. *F*, schematic representation of dual recordings from a D-IN (orange, top), a

S-IN (magenta, bottom) and a GC (black) in the dorsal DG upon photostimulation of ventral MC terminals. *G*, top, representative morphological reconstruction of a recorded D-IN (axons in red; soma and dendrites in orange) and a GC (black) and their respective firing patterns. The averaged EPSC traces of the D-IN (orange) and GC (black) are shown. Bottom, representative morphological reconstruction of the recorded S-IN (axons in red; soma and dendrites in magenta) and GC (black) and their respective firing patterns. The averaged EPSC traces of the S-IN (magenta) and GC (black) obtained in the dorsal DG are shown. *H*, summary of ventral MC → dorsal DG mediated $EPSG_1$ in D-INs and GCs (top) and S-INs and GCs (bottom). The connected lines represent the neurons obtained from the same slice. For D-INs and GCs, n = 12 cells from 11 mice (Mann–Whitney test; P = 0.8729; U = 32.50). For S-INs and GCs, n = 5 cells from 5 mice (Mann–Whitney test; P = 0.056; U = 3.00). Error bars indicate the SD. DG, dentate gyrus; D-IN, dendrite-targeting interneurons; EPSG, excitatory postsynaptic conductance; GC, granule cell; MC, mossy cell; S-IN, soma-targeting interneurons.

Table 2. Properties of ventral MC → ventral IN and ventral MC → dorsal IN synapses

	Ventral IN	Dorsal IN	*P*
D-IN			
EPSC (pA)	340.5 ± 62.4 (18)	175.4 ± 59.6 (12)	<0.05
EPSG (nS)[a]	4.5 ± 0.8 (18)	2.3 ± 0.7 (12)	<0.05
Q_{EPSC} (pC)	3.5 ± 0.7 (18)	1.5 ± 0.6 (12)	<0.05
Latency (ms)	3.1 ± 0.1 (18)	3.1 ± 0.3 (12)	0.84
A_f (pA)	29.4 ± 7.2 (18)	9.2 ± 4.4 (12)	<0.05
A_s (pA)	339.6 ± 67.0 (18)	195.2 ± 63.4 (12)	0.13
τ_f (ms)	88.6 ± 24.1 (18)	62.6 ± 14.2 (12)	0.90
τ_s (ms)	6.4 ± 0.4 (18)	7.4 ± 0.9 (12)	0.63
EPSC τ_w (ms)	11.8 ± 1.4 (18)	10.3 ± 3.1 (12)	0.14
S-IN			
EPSC (pA)	219.4 ± 58.7 (5)	54.6 ± 16.6 (5)	<0.05
EPSG (nS)[a]	3.0 ± 0.8 (5)	0.7 ± 0.2 (5)	<0.05
Q_{EPSC} (pC)	2.4 ± 0.9 (5)	0.8 ± 0.3 (5)	<0.05
Latency (ms)	2.5 ± 0.2 (5)	2.9 ± 0.4 (5)	0.51
A_f (pA)	10.9 ± 1.9 (5)	3.8 ± 1.9 (5)	0.09
A_s (pA)	230.8 ± 62.9 (5)	55.6 ± 16.2 (5)	<0.05
τ_f (ms)	6.4 ± 0.9 (5)	8.8 ± 1.9 (5)	0.40
τ_s (ms)	114.7 ± 66.0 (5)	128.3 ± 28.1 (5)	0.41
EPSC τ_w (ms)	12.4 ± 3.8 (5)	14.3 ± 3.9 (5)	0.66

Data were obtained in the whole-cell voltage-clamp mode at ∼23°C. Mann–Whitney test was performed to compare means between the groups. Values in parentheses indicate the total number of cells for each group.
[a]The EPSG was calculated from the first EPSC shown in Fig. 5.

& Kosaka, 1999; Fujise et al., 1998; Houser et al., 2021; Jinno et al., 2003; Scharfman, 2016; Scharfman & Myers, 2013). Here, we assessed whether dorsal MC connections differed from ventral MC connections. We selectively expressed ChR2 in dorsal MCs and recorded EPSCs and IPSCs from local and distant GCs. Following the activation of dorsal MCs, fast EPSCs and slow IPSCs were recorded from local (dorsal) GCs (Fig. 6*A* and *B*). The inhibitory conductance was significantly higher than excitatory conductance (Fig. 6*C* and *D*) and the E/I ratio for the first stimulus was significantly <1 during the 5-Hz stimulation of MCs (Fig. 6*E*). Similar experiments were conducted on distant (ventral) DG slices (Fig. 6*F* and *G*). Consistent with our observation in the ventral MC connections, the excitatory conductance was significantly higher than the inhibitory conductance (Fig. 6*G–I*) and the E/I ratios were significantly >1 (Fig. 6*J*). However, in striking contrast to our observation in the ventral MC connections, our data revealed that the EPSGs at dorsal MC projections were significantly greater in the distant GCs (i.e. ventral GCs) than in the local GCs (Fig. 6*K* and *M*), whereas equivalent IPSGs were detected between intralamellar (dorsal GC; n = 8 from 4 mice) and trans-lamellar (ventral GC; n = 8 from 4 mice) GCs (Fig. 6*L* and *M*). Taken together, these findings revealed that MC-mediated low or high E/I balance in local or distant GCs was maintained through distinct mechanisms along the ventrodorsal and dorsoventral axes (Figs 4*O* and 6*M*).

Ventral MCs differentially regulate E/I balance in contralateral ventral and dorsal GCs

Finally, we attempted to investigate the properties of MC connectivity with the commissural ventral and dorsal GCs

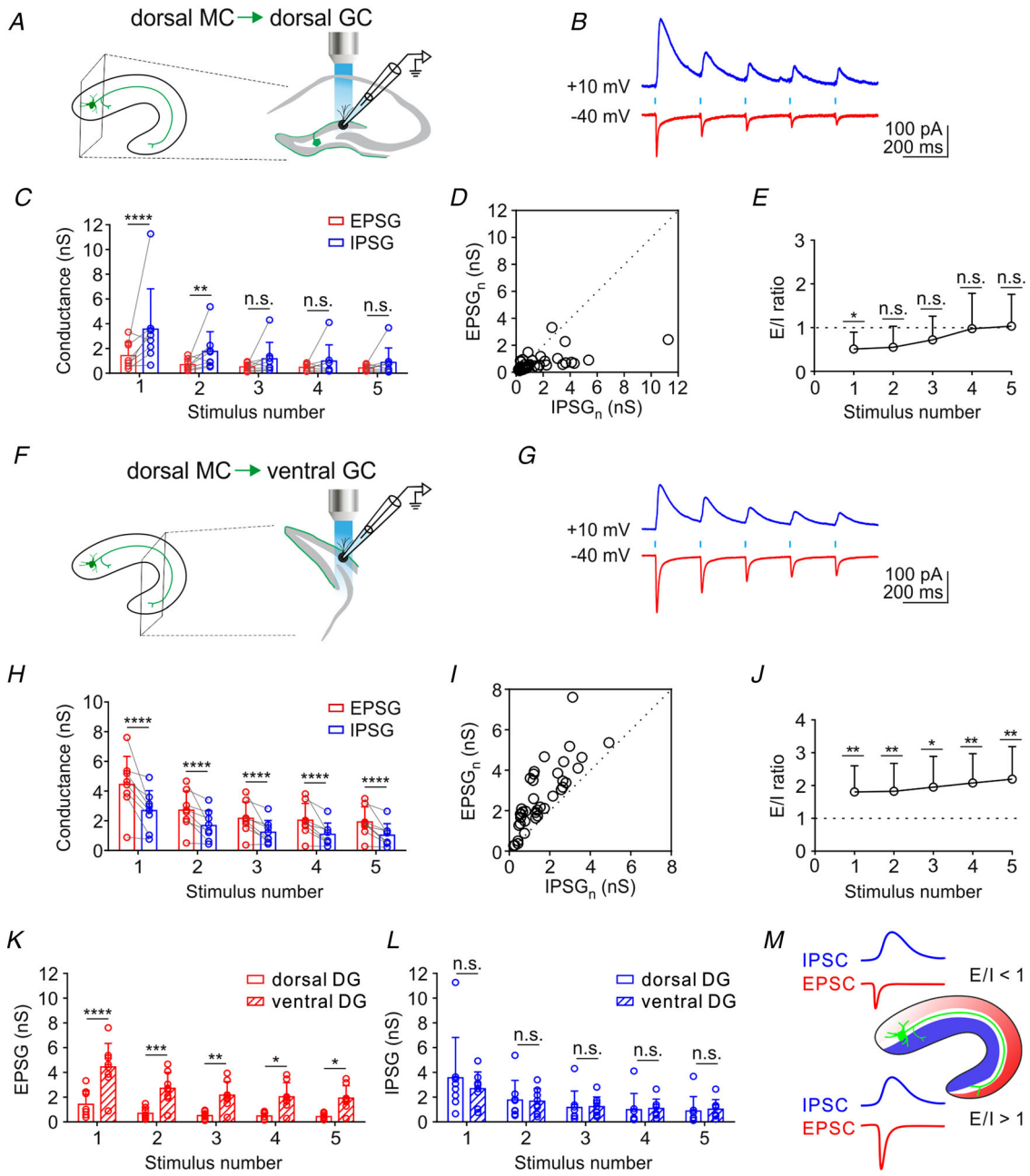

Figure 6. Activating dorsal MCs induces a low E/I balance in dorsal GCs and a high E/I balance in ventral GCs

A, experimental schematic representation of whole-cell voltage-clamp recording from a dorsal GC. *B*, averaged traces of EPSC (red; V_{hold} = −40 mV) and IPSC (blue; V_{hold} = +10 mV) of a dorsal GC in response to 5-Hz photostimulation of dorsal MCs. *C*, summary plot of EPSGs and IPSGs in response to 5-Hz photostimulation; n = 8 cells from 4 mice (two-way repeated measures ANOVA with the Bonferroni *post hoc* test; $P < 0.0001$, $P = 0.0035$, $P = 0.1440$, $P = 0.4226$ and $P = 0.6071$ for stimulus nos 1–5, respectively). *D*, distribution of EPSGs and IPSGs of dorsal GCs in response to 5-Hz photostimulation of dorsal MCs; n = 40 from 8 cells and 4 mice. *E*, summary of the E/I ratio *versus* the stimulus number of dorsal GCs in response to 5-Hz photostimulation of dorsal MCs; n = 8 cells from 4 mice (Wilcoxon signed-rank test against 1; $P = 0.0234$, $P = 0.0781$, $P = 0.1953$, $P = 0.5469$ and $P = 1.0000$ for stimulus nos 1–5, respectively). *F*, experimental schematic representation of whole-cell voltage-clamp recording from a ventral GC. *G*, averaged traces of EPSC (red; V_{hold} = −40 mV) and IPSC (blue; V_{hold} = +10 mV) of a ventral GC in response to 5-Hz photostimulation of dorsal MC terminals. *H*, summary plot of EPSGs and IPSGs in response to 5-Hz photostimulation; n = 8 cells from 4 mice (two-way repeated measures ANOVA with the Bonferroni *post hoc* test; all $P < 0.0001$). *I*, distribution of EPSGs and IPSGs of ventral GCs in response to 5-Hz photostimulation of dorsal MC terminals; n = 40 from 8 cells and 4 mice. *J*, summary of the E/I ratio *versus* the stimulus number

of ventral GCs in response to 5-Hz photostimulation of dorsal MC terminals; n = 8 cells from 4 mice (Wilcoxon signed-rank test against 1; P = 0.0078 for stimulus nos 1, 2, 4 and 5, respectively, and P = 0.0156 for stimulus no. 3). *K*, summary of dorsal MC → dorsal DG (n = 8 from 4 mice) and dorsal MC → ventral DG (n = 8 from 4 mice) pathway-mediated EPSGs in GCs (two-way ANOVA with the Bonferroni *post hoc* test; $P < 0.0001$, P = 0.0009, P = 0.0096, P = 0.0163 and P = 0.0231 for stimulus nos 1–5, respectively). *L*, summary of dorsal MC → dorsal DG and dorsal MC → ventral DG pathway-mediated IPSGs in GCs (two-way ANOVA with the Bonferroni *post hoc* test; all $P > 0.9999$). *M*, schematic representation showing that in dorsal MC → ventral DG pathway, the inhibitory response (IPSG) is similar between the dorsal GCs and ventral GCs while the excitatory response is larger at the dorsal MC → ventral GC synapses. All error bars indicate the SD. DG, dentate gyrus; EPSC, excitatory postsynaptic current; EPSG, excitatory postsynaptic conductance; GC, granule cell; IPSC, inhibitory postsynaptic current; IPSG, inhibitory postsynaptic conductance; MC, mossy cell.

in unilaterally injected mice (Fig. 7*A* and *F*). In the ventral MC → commissural ventral GC connection, we observed that the inhibitory conductance was mostly higher than the excitatory conductance (Fig. 7*B–D*; $n = 14$ cells from 5 mice), and the E/I ratios at ventral MC → commissural ventral GC projections were significantly <1 for the first and second stimuli and were close to 1 for the subsequent stimuli (Fig. 7*E*). This was consistent with our previous finding (Hsu et al., 2016) that MC commissural connections with GCs in the dorsal DG are primarily inhibitory (low E/I balance). Interestingly, at the ventral MC → commissural dorsal GC synapses, excitatory and inhibitory conductances were not significantly different (Fig. 7*G–I*; $n = 10$ cells from 5 mice) and the E/I ratios were close to 1 during repetitive photostimulation (Fig. 7*J*). Taken together, our data revealed MCs mediate lamellar and hemispheric specific E/I balance along the hippocampal longitudinal axis.

Table 3. Synaptic potentials of ventral MC → ventral GC and ventral MC → dorsal GC connections

	Ventral GC (n = 12)	Dorsal GC (n = 11)	P
PSP Amp. (mV)	9.4 ± 2.3	15.0 ± 2.9	0.07
20–80% rise time (ms)	2.0 ± 0.2	2.2 ± 0.3	0.67
PSP decay τ (ms)	21.0 ± 1.3	43.3 ± 4.0	<0.05
Charge transfer (pC)[a]	0.2 ± 0.1	0.6 ± 0.1	<0.05

Data were obtained in the whole-cell voltage-clamp configuration at ∼23°C. The results were compared using the Mann–Whitney test. Values in parentheses indicate the total number of cells.
[a]The charge transfer was measured as an integral area under the postsynaptic potential (PSP).

MC activation regulates local and distant GC activities differentially

In slices, GCs received reduced excitatory drives. Therefore, photostimulation of MCs alone in slices was insufficient to reliably evoke GC firing (unpublished observation). To test whether activation of ventral MCs could modulate action potential generation in GCs in the ventral DG and dorsal DG, we delivered steps of 5-Hz sinusoidal currents in ventral and dorsal GCs and later paired this with a 5-Hz light stimulation of MC terminals at different intervals (Fig. 8*A* and *F*). The light stimulation occurred either close to the peak of the sine waveform (Δt = ∼0 ms; Fig. 8*A*, right) or preceded the peak of the sine waveform by ∼30 ms (Fig. 8*A*, right). The light stimulation alone caused postsynaptic responses in ventral GCs at −75 mV (Fig. 8*B*; Table 3). The results showed that the photostimulation of ventral MCs near the peak of the sine waveform ($\Delta t = 1.2$ ms) increased the spike number in ventral GCs (Fig. 8*B* and *C*; $n = 5$ cells from 4 mice). In contrast, when the photostimulation preceded the peak of sine waveform by 28.8 ms, activation of ventral MCs significantly reduced the spike number in ventral GCs (Fig. 8*D* and *E*; $n = 7$ cells from 4 mice). This finding further corroborates our finding that the feedforward inhibitory response dominates at the ventral MC → ventral GC connection. Similar experiments were conducted in dorsal GCs. Activation of ventral MC terminals near the peak of the sine waveform ($\Delta t = 1.2$ ms) caused a significant increase in the spike number of dorsal GCs (Fig. 8*G* and *H*; $n = 6$ cells from 3 mice). However, in striking contrast to that of the local GCs, activation of ventral MC terminals ∼30 ms (Δt = 28.8 ms) before the peak of the sine waveform still caused a significant increase in the spike number in dorsal GCs (Fig. 8*I* and *J*; $n = 5$ cells from 4 mice). This finding supports the perspective that the MC-mediated feedforward inhibitory effect is too weak to override the MC-mediated excitatory effect of MCs on dorsal GCs. Taken together, our results showed that MC activation can differentially control action potential generation in ventral and dorsal GCs.

MC activation regulates spike timing in local and distant GCs differentially

Synaptic inhibition can enhance the spike-timing precision by curtailing excitatory postsynaptic potentials (EPSPs) (Pouille & Scanziani, 2001). Several studies suggested that MC-mediated transmission in the same

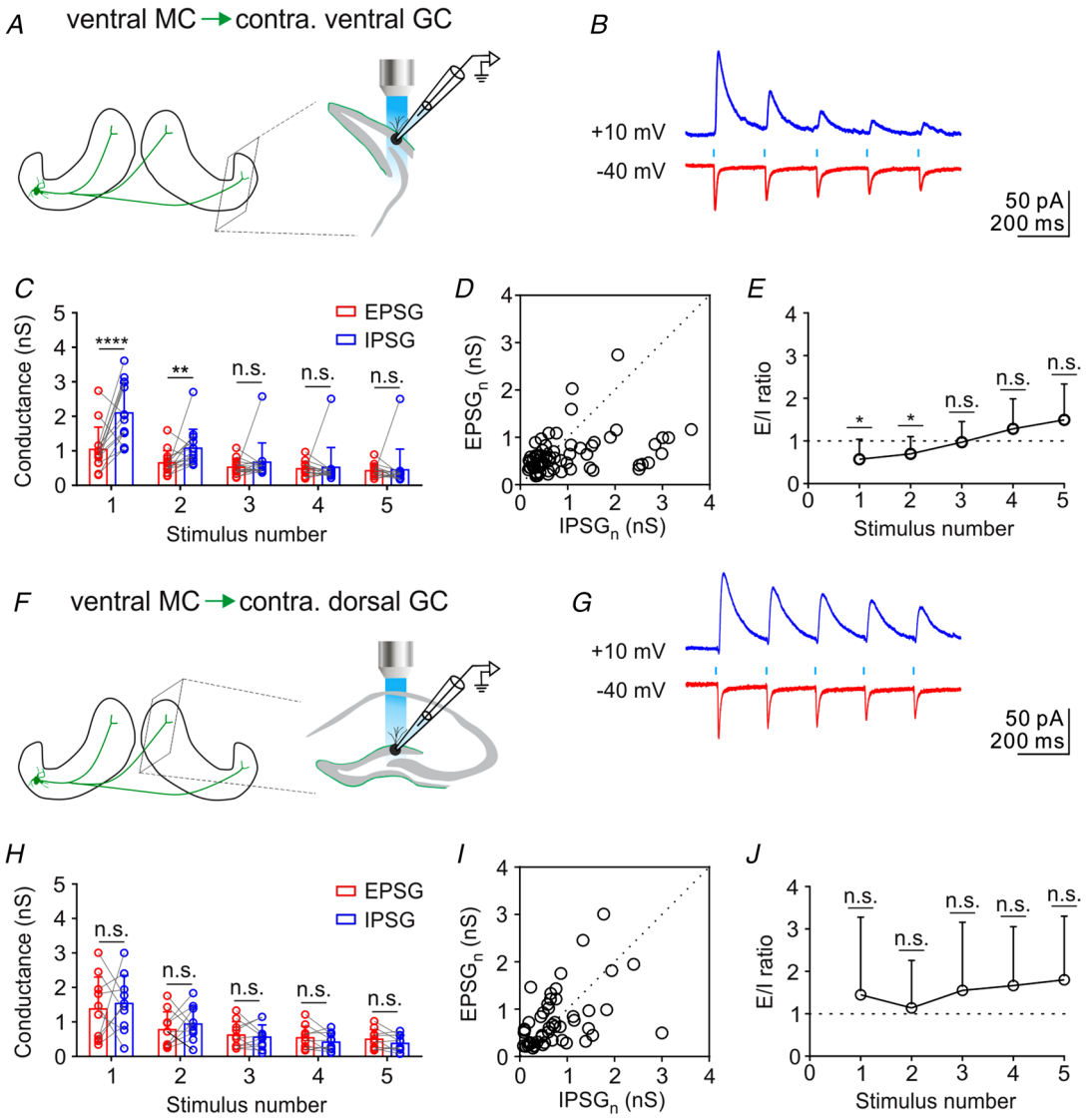

Figure 7. Activating commissural projections of ventral MCs induces differential E/I balance in contralateral ventral GCs and dorsal GCs
A, experimental schematic representation of whole-cell voltage-clamp recording from a contralateral ventral GC. *B*, averaged traces of EPSC (red; V_{hold} = −40 mV) and IPSC (blue; V_{hold} = +10 mV) of a contralateral ventral GC in response to 5-Hz photostimulation of ventral MC terminals. *C*, summary plot of EPSGs and IPSGs of contralateral ventral GCs in response to 5-Hz photostimulation of ventral MC terminals; n = 14 cells from 5 mice (two-way repeated measures ANOVA with the Bonferroni *post hoc* test; $P < 0.0001$, $P = 0.0025$ for stimulus nos 1 and 2, respectively, $P > 0.9999$ for stimulus nos 3–5). *D*, distribution of EPSGs and IPSGs of contralateral ventral GCs in response to 5-Hz photostimulation of ventral MC terminals; n = 70 from 14 cells and 5 mice. *E*, summary plot of the E/I ratio *versus* the stimulus number of contralateral ventral GCs in response to 5-Hz photostimulation of ventral MC terminals; n = 14 cells from 5 mice (Wilcoxon signed-rank test against 1; $P = 0.0166$ for stimulus nos 1 and 2, respectively, $P = 0.8077$, $P = 0.1726$ and $P = 0.0676$ for stimulus nos 3–5, respectively). *F*, experimental schematic representation of whole-cell voltage-clamp recording from a contralateral dorsal GC. *G*, averaged traces of EPSC (red; V_{hold} = −40 mV) and IPSC (blue; V_{hold} = +10 mV) of a contralateral dorsal GC in response to 5-Hz photostimulation of ventral MC terminals. *H*, summary plot of EPSGs and IPSGs of contralateral dorsal GCs in response to 5-Hz photostimulation of ventral MC terminals; n = 10 cells from 5 mice (two-way repeated measures ANOVA with the Bonferroni *post hoc* test; all $P > 0.9999$). *I*, distribution of EPSGs and IPSGs of contralateral dorsal GCs in response to 5-Hz photostimulation of ventral MC terminals; n = 50 from 10 cells and 5 mice. *J*, summary plot of the E/I ratio *versus* the stimulus number of contralateral dorsal GCs in response to 5-Hz photostimulation of ventral MC terminals; n = 10 cells from 5 mice (Wilcoxon signed-rank test against 1; $P = 1.0000$ for stimulus nos 1 and 2, $P = 0.6250$, $P = 0.1602$ and $P = 0.1055$ for stimulus nos 3–5, respectively). EPSG, excitatory postsynaptic conductance; GC, granule cell; IPSG, inhibitory postsynaptic conductance; MC, mossy cell.

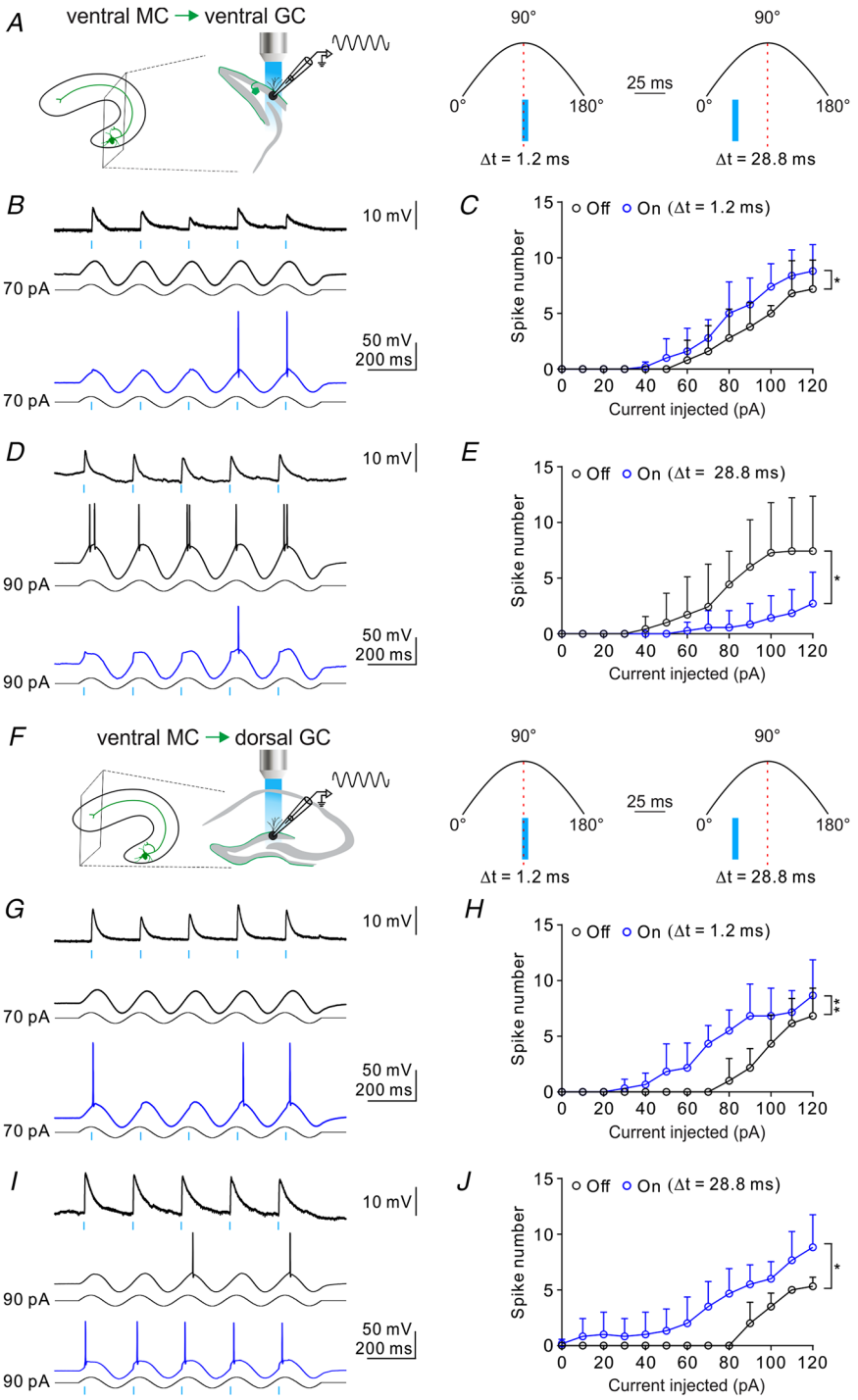

Figure 8. MCs differentially modulate ventral and dorsal GC activity
A, left, experimental schematic representation for ventral MC → ventral GC connections. Steps of sinusoidal current were delivered to induce GC firing. Right, red dotted lines represent the peaks of the sinusoidal waveform ($t = 0$ ms). Blue bars represent the periods of photostimulation (left, $\Delta t = 1.2$ ms; right, $\Delta t = 28.2$ ms). *B*, top, the postsynaptic potentials recorded in a ventral GC at −75 mV in current clamp in response to photostimulation of ventral MCs. Middle, the representative trace responds to 70 pA of 5-Hz sinusoidal current injection without the photostimulation of ventral MCs. Bottom, the pairing of 5-Hz photostimulation of ventral MCs with 70 pA of 5-Hz sinusoidal current injection; $\Delta t = 1.2$ ms between onset of photostimulation of ventral MCs and the peak of sinusoidal current. *C*, summary plot of spike number *versus* steps of sinusoidal current. Photostimulation of ventral MCs significantly increases the spike number in ventral GCs. $n = 5$ from 4 mice (two-way repeated measures ANOVA, $F_{(1,4)} = 11.12$, $P = 0.029$). *D*, similar to *B*. Top, the postsynaptic potentials recorded in a ventral GC at −75 mV in current-clamp. The

representative traces respond to 90 pA of 5-Hz sinusoidal current injection without (middle) and with (bottom) the photostimulation of ventral MCs. $\Delta t = 28.2$ ms between photostimulation of ventral MCs and the peak of sinusoidal current. *E*, similar to *C*, plot of spike number *versus* steps of sinusoidal current in ventral GCs with $\Delta t = 28.2$ ms; $n = 7$ cells from 4 mice (two-way repeated measures ANOVA, $F_{(1,6)} = 8.641$, $P = 0.026$). *F*, experimental schematic representation of the ventral MC → dorsal GC connections. Steps of sinusoidal current were injected to induce GC firing. Red dotted lines represent the peaks of the sinusoidal waveform ($t = 0$ ms). Blue bars represent the periods of photostimulation of ventral MC terminals (left, $\Delta t = 1.2$ ms; right, $\Delta t = 28.2$ ms). *G*, top, the post-synaptic potentials recorded in a dorsal GC at −75 mV in current clamp in response to photostimulation of ventral MC terminals. Middle, the representative trace response to 70 pA of 5-Hz sinusoidal current injection without the photostimulation of MC terminals. Bottom, the pairing of 5-Hz photostimulation of ventral MC terminals with 70 pA of 5-Hz sinusoidal current injection; $\Delta t = 1.2$ ms between photostimulation of ventral MC terminals and the peak of sinusoidal current. *H*, summary plot of spike number *versus* steps of sinusoidal current. Photostimulation of ventral MC terminals significantly increases the spike number in dorsal GCs. $n = 6$ from 3 mice (two-way repeated measures ANOVA, $F_{(1,5)} = 33.36$, $P = 0.002$). *I*, similar to *G*, the postsynaptic potentials recorded in a dorsal GC at −75 mV in current clamp. The representative traces respond to 90 pA of 5-Hz sinusoidal current injection without (middle) and with (bottom) the photostimulation of ventral MC terminals. $\Delta t = 28.2$ ms between photostimulation of ventral MC terminals and the peak of sinusoidal currents. *J*, similar to *H*, plot of spike number *versus* steps of sinusoidal current in dorsal GCs with $\Delta t = 28.2$ ms; $n = 6$ from 3 mice (two-way repeated measures ANOVA, $F_{(1,5)} = 7.863$, $P = 0.0378$). Error bars indicate the SD. Also see Table 3, for comparison of postsynaptic potentials in ventral GCs and dorsal GC. GC, granule cell; MC, mossy cell.

lamella differs from that in translamellae (Buckmaster et al., 1992, 1996; Scharfman, 2016; Scharfman & Myers, 2013). Indeed, in contrast to the excitatory effect on local GCs, activation of MCs can exert inhibitory effects on local GCs. Therefore, we assessed whether MCs differentially regulate the spike timing of GCs along the longitudinal axis. To test this, we applied a 5-Hz sinusoidal current injection protocol to induce GC firing (Hu et al., 2009; Hutcheon & Yarom, 2000; Pernía-Andrade & Jonas, 2014). Firing of MCs under *in vivo* conditions is phase-locked to the theta rhythm (Botterill et al., 2019; Henze & Buzsáki, 2007; Senzai & Buzsáki, 2017; Soltesz et al., 1993). To investigate the effect of MC activation on GC spiking, we paired an optical stimulation of MC terminals with current injection in recorded GCs (Fig. 9*A*). As exemplified, we examined the timing of action potentials in ventral GCs with and without activation of MC terminals (Fig. 9*B*). Compared to the light-off epoch (Fig. 9*B*, top traces), superimposed spike trains from a GC showed that spikes occurred earlier, and more precisely in time during the light-on session (Fig. 9*B*, bottom traces). The plots showed a significant decrease in the phase angle (spike timing/latency, Fig. 9*C*) and spike jitter (Fig. 9*D*) during MC activation ($n = 9$ cells from 5 mice). The most pronounced effect on spike jitter was observed during the first burst (Fig. 9*D*). Interestingly, by conducting the same experiment in dorsal GCs (i.e. the dorsal DG; Fig. 9*E*; $n = 8$ cells from 5 mice), we found that activation of the MC terminals only reduced the spike latencies in translamellar GCs (Fig. 9*F* and *G*), but did not cause a significant decrease in the spike jitter (Fig. 9*H*). Taken together, these results suggested that MC associational axonal projections regulate intralamellar and translamellar GC activities differentially.

Modulatory effect of MCs on distant GC activity

Finally, we examined whether the long-projecting axonal collaterals of MCs exert any impact on GC activity in the distal pole. To this end, we recorded the GC population response to activation of ventral MC terminals and/or the medial perforant path (MPP) fibres, the primary cortical input from the medial entorhinal cortex to the DG (Fig. 10*A*). Photo-stimulation of ChR2-expressing ventral MC collaterals induced the field excitatory post-synaptic potential (fEPSP) (Fig. 10*B* top, green trace). Similarly, activation of the MPP with suprathreshold electrical stimulation evoked the fEPSP and population spike (pSpike) (Fig. 10*B* top, black trace). The area under the pSpike is regarded as a measure of the number of GCs that spike synchronously to the input stimulus (Hsu et al., 2016; Lee et al., 2016; Temprana et al. 2015). By co-activating both inputs, we tested the collateral effect of the ventral MCs on the GC pSpike in the dorsal DG. Notably, concurrent activation of ventral MC terminals by photo-stimulation increased the pSpike area (Fig. 10*B* top, blue trace). Enhancement of pSpike area was observed in the five recordings ($n = 5$ slices from 3 mice). This was significant for all stimulations, that is, nos 1–5. Similarly, MPP-induced pSpikes were enhanced by co-activation of ventral MC collaterals when bursts of five electrical shocks were applied to the MPP at a behaviourally relevant frequency, i.e. 5 Hz ($n = 5$ slices from 3 mice; Fig. 10*B*, middle traces and *C*). However, when the ventral MC activation preceded the PP activation by 10 ms (Fig. 10*B* top, light blue trace), there was no significant change in pSpike areas in response to MPP activation ($n = 5$ slices from 3 mice; Fig. 10*B*, bottom traces and *C*). This result was in great contrast to the regulation of MPP input efficacy at ventral MC → local GC connections (Fig. 11). When we recorded the response of ventral GCs

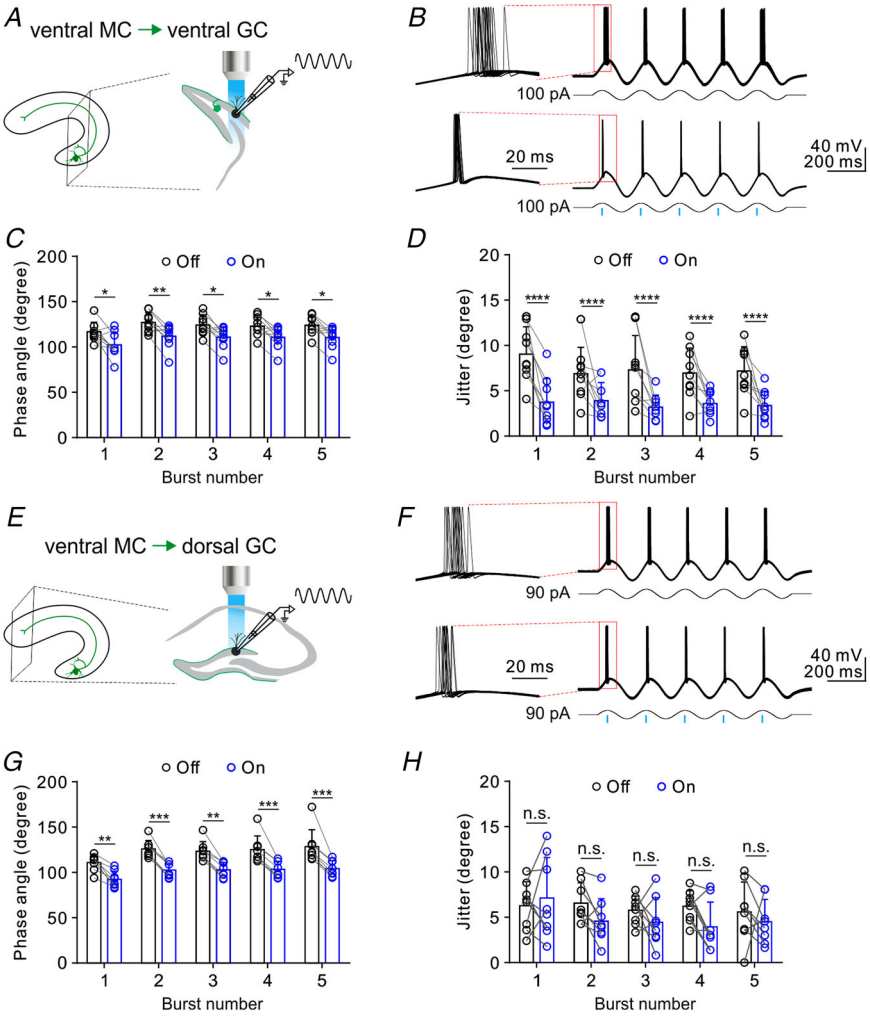

Figure 9. MC activation differentially regulates spike timing of ventral and dorsal GCs
A, experimental schematic representation showing ChR2-eYFP-expressing cells in the hilus and axons in the IML (green) of ventral DG. Whole-cell patch-clamp recording was made from a ventral GC. 5-Hz sinusoidal current was injected to induce GC firing and blue light to activate ventral MCs. *B*, top, overlay of spikes generated by 5-Hz sinusoidal current injection in a ventral GC at −75 mV in current-clamp during 20 sweeps/trials without the photostimulation of ventral MCs. Bottom, same as the top but paired with 5-Hz photostimulation of ventral MCs. *C*, summary plot of phase angles (latencies) against the burst number; $n = 9$ cells from 5 mice (two-way repeated measures ANOVA with the Bonferroni *post hoc* test; $P = 0.0123$, $P = 0.0083$, $P = 0.0230$, $P = 0.0409$ and $P = 0.0223$ for burst nos 1–5, respectively). *D*, summary of spike jitter against the burst number. Photostimulation of ventral MCs significantly reduces spike jitter in ventral GCs; $n = 9$ cells from 5 mice (two-way repeated measures ANOVA with the Bonferroni *post hoc* test; all $P < 0.0001$ for burst nos 1–5). *E*, experimental schematic representation showing ChR2-eYFP expression in the IML (green) of dorsal DG. Whole-cell patch-clamp recording was made from a dorsal GC. 5-Hz sinusoidal current was injected to induce GC firing and blue light was delivered to activate ventral MC axons. *F*, top, overlay of spikes generated by 5-Hz sinusoidal current injection in a dorsal GC at −75 mV in current-clamp during 20 sweeps/trials. Bottom, same as the top, but paired with 5-Hz photostimulation of ventral MC terminals. *G*, summary plot of phase angles (latencies) against the burst number; $n = 8$ cells from 5 mice (two-way repeated measures ANOVA with the Bonferroni *post hoc* test; $P = 0.0063$, $P = 0.0004$, $P = 0.0019$, $P = 0.0009$ and $P = 0.0002$ for burst nos 1–5, respectively). *H*, summary of spike jitter against the burst number. Photostimulation of ventral MC axons did not show a significant effect on spike jitter in dorsal GCs; $n = 8$ cells from 5 mice (two-way repeated measures ANOVA with the Bonferroni *post hoc* test; $P > 0.9999$, $P = 0.2976$, $P > 0.9999$, $P = 0.1564$ and $P > 0.9999$ for bursts nos 1–5, respectively). Error bars indicate the SD. GC, granule cell; MC, mossy cell.

(local GCs) to MPP activation (Fig. 11*A*–*C*), we found that MPP-induced pSpikes were enhanced by co-activation of ventral MCs when bursts of five electrical shocks were applied to the MPP at 5 Hz ($n = 6$ slices from 3 mice; Fig. 11*B*, middle traces and *C*). However, when the ventral MC activation preceded the MPP activation by 10 ms, there was a significant decrease in pSpike areas ($n = 6$ slices from 3 mice; Fig. 11*B*, bottom traces and *C*), suggesting a significant inhibitory conductance underlying MC → local GC connections ($n = 6$ slices from 3 mice; Fig. 11*B* and *C*). Taken together, our results indicate that activation of ventral MCs differentially modulates the response of GCs to the cortical input along the hippocampal long axis.

Discussion

According to the GC association hypothesis (Buckmaster & Schwartzkroin, 1994), coupling of two physically separated GC populations via MC associational axonal projections is instrumental for information processing. In this study, we showed that MCs establish a distinct and opposite synaptic E/I balance at synapses in the local and distal areas of the hippocampus and exert the collateral effect on distant GCs. Based on our experiments, we propose that the intrahippocampal long axis circuitry plays a role in associative contextual learning. When an animal explores a new environment with a salient cue, the context input 'Y' such as spatial information to the dorsal DG and the salient cue input 'X' such as the

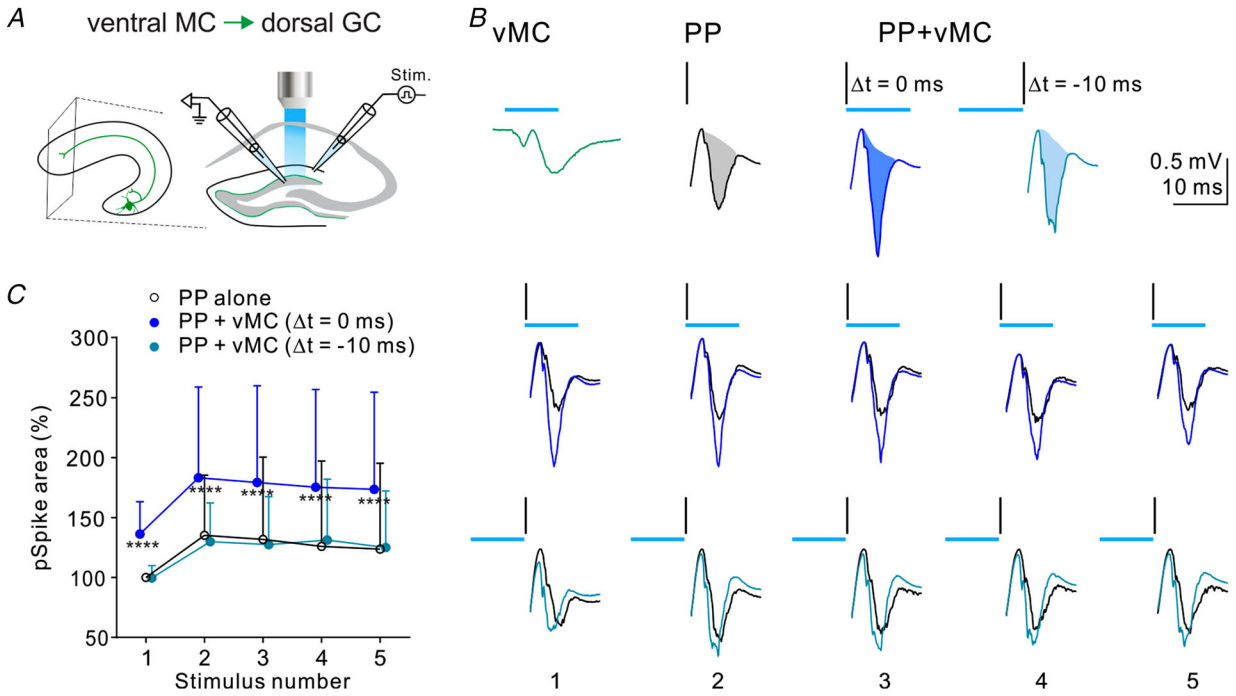

Figure 10. Effect of the ventro-dorsal hippocampal connection on dorsal GC activity
A, schematic representation of the experimental configuration. A field recording electrode was placed in the dorsal GCL to monitor fEPSPs and pSpikes. A stimulation electrode was placed in the MML to activate the MPP; the ChR2-expressing axonal collateral fibres of the ventral MCs (green) were stimulated with blue light emitted through the objective. *B*, top, light-evoked response (green), consisting of the fibre volley followed by the fEPSP. Black trace, pSpike in response to the MPP stimulation alone. The vertical bar represents a single electrical stimulating pulse. Blue trace, co-activation of MPP and ventral MC terminals (blue, $\Delta t = 0$ ms). Cyan trace, activation of ventral MC terminals precedes the MPP stimulation (cyan, $\Delta t = -10$ ms). Grey, blue and cyan areas indicate the areas under the pSpikes. Bottom, five consecutive pSpike responses to the MPP alone and co-activation of MPP and ventral MC terminals. Traces of pSpike correspond to the stimulus number. The stimulation frequency is 5 Hz. Black traces, the MPP stimulation alone. Blue traces, co-activation of the MPP and ventral MC terminals ($\Delta t = 0$ ms). Cyan traces, activation of the MPP and ventral MC terminals ($\Delta t = -10$ ms). *C*, summary of the effect of ventral MC collateral activation on pSpike area. The magnitude of pSpike area (normalized to the first pSpike area to the MPP stimulation alone) was plotted against the stimulation number. Data represent averaged recording from 5 slices and 3 mice). Co-activation ($\Delta t = 0$ ms) of the ventral MC terminals and MPP significantly increased the pSpike area (two-way repeated measures ANOVA with the Bonferroni *post hoc* test, $F_{(1,4)} = 18.99$; all $P < 0.0001$). Pre-activation of ventral MC terminals ($\Delta t = -10$ ms) did not have a significant effect on pSpike area (two-way repeated measures ANOVA with the Bonferroni *post hoc* test, $F_{(1,4)} = 0.0026$; all $P > 0.9999$). Error bars indicate the SD. fEPSP, field electrical postsynaptic potential; GC, granule cell; GCL, granule cell layer; MC, mossy cell; MML, middle molecular layer; MPP, medial perforant path; pSpike, population spike.

novelty signal to the ventral DG can activate dorsal GCs and ventral GCs, respectively (Fig. 12). Via GC mossy fibre collaterals, ventral GCs drive ventral MCs, which project associational axonal collaterals to the proximal dendrites of GCs and INs in the dorsal DG. The input from ventral MCs to the dorsal GC is predominantly excitatory (E/I >1) and thus the postsynaptic potential (PSP) is slow decaying. Therefore, the salient cue input 'X' can potentiate the effect of the context input 'Y'. The input of associational axonal collaterals from ventral MCs serves as a teaching signal during associative contextual learning. The collateral effect produced by the MC axonal projections is required for novelty-induced contextual memory formation (Bauer et al., 2021; Fredes et al., 2021; Fredes & Shigemoto, 2021).

It is noteworthy that Jinde et al. (2013) proposed that MCs provide feedforward inhibition on intralamellar and translamellar GCs via two distinct IN subpopulations. According to their model, MCs activate D-INs with slow-rise kinetics, such as the molecular layer perforant path-associated (aka, MOPP) cells within the same lamella, while activating S-INs with fast-rise kinetics, for example, the basket cells in the distant lamellae, which provide strong lateral inhibition on GCs. However, this speculative view is in contrast with certain anatomical observations implying that basket cells are not the major target of MCs in distant lamellae (Blasco-Ibáñez & Freund, 1997; Buckmaster et al., 1992, 1996). Our study shows that both S-INs and D-INs in the dorsal DG are subjected to weaker excitatory transmission by ventral MCs

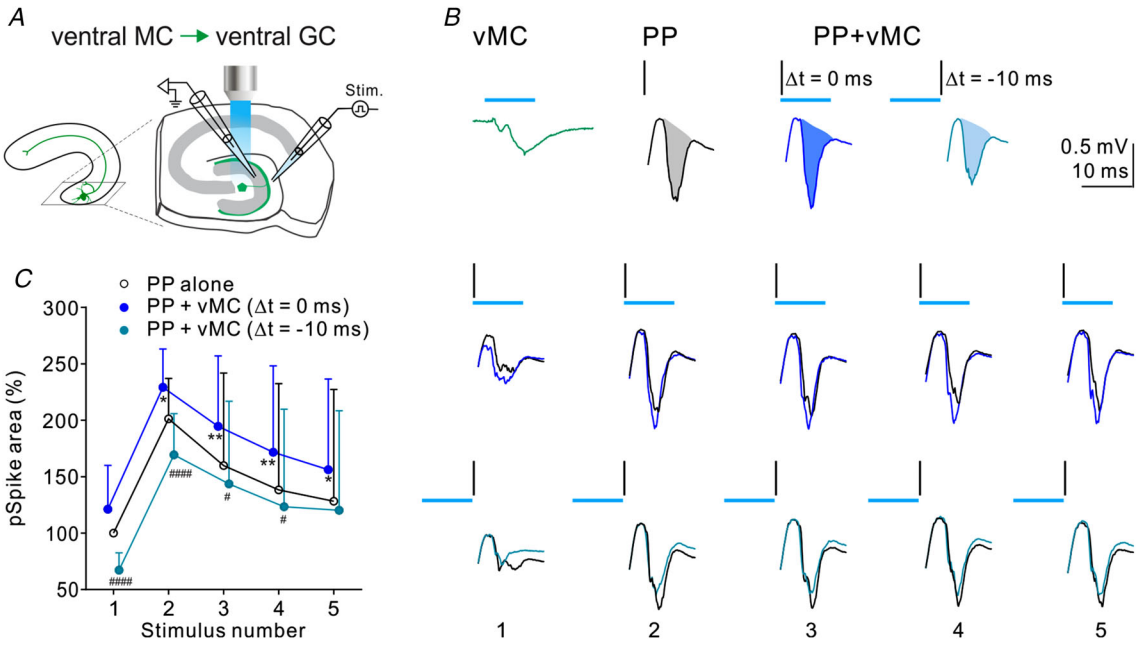

Figure 11. Effect of the ventral MC activation on MPP-induced pSpikes in ventral GCs
A, schematic representation of experimental configuration: a field recording electrode was placed in the ventral GCL to monitor fEPSPs and pSpikes. A stimulation electrode was placed in the MML to activate the MPP; ventral MCs (green) expressing ChR2 were stimulated with blue light emitted through the objective. *B*, top, light-evoked response (green), consisting of the fibre volley followed by the light-evoked fEPSP. Black trace, pSpike response to the MPP stimulation alone. Vertical bar represents a single electrical stimulating pulse. Blue trace, co-activation of MPP and ventral MC terminals (blue, Δt = 0 ms). Cyan trace, activation of ventral MC terminals precedes the MPP stimulation (cyan, Δt = −10 ms). Grey, blue and cyan areas indicate the areas under the pSpikes. Bottom, five consecutive pSpike responses to the MPP alone and co-activation of MPP and ventral MCs. Traces of pSpike corresponding to the stimulus number. The stimulation frequency is 5 Hz. Black traces, MPP stimulation alone. Blue traces, co-activation of MPP and ventral MC (Δt = 0 ms). Cyan traces, activation of MPP and ventral MCs (Δt = −10 ms). *C*, summary of effect of ventral MC activation on pSpike area in the ventral DG. The magnitude of pSpike area (normalized to the first pSpike area to the MPP stimulation alone) was plotted against the stimulation number. Data represent averaged recording from 6 slices and 3 mice. Co-activation (Δt = 0 ms) of ventral MCs mostly increased the pSpike (two-way repeated measures ANOVA with the Bonferroni *post hoc* test, $F_{(1,5)}$ = 2.745; P = 0.1115; P = 0.0187, P = 0.0030, P = 0.0045 and P = 0.0193 for stimulation nos 1–5, respectively). In contrast, pre-activation of ventral MCs (Δt = −10 ms) mostly reduced the pSpike area (two-way repeated measures ANOVA with the Bonferroni *post hoc* test, $F_{(1,5)}$ = 5.213; $^{\#\#\#\#}P < 0.0001$ for stimulus nos 1 and 2, $^{\#}P$ = 0.0129, $^{\#}P$ = 0.0238, and P = 0.5171 for stimulus nos 3–5, respectively). Error bars indicate the SD. fEPSP, field excitatory postsynaptic potential; GC, granule cell; GCL, granule cell layer; MC, mossy cell; MML, middle molecular layer; MPP, medial perforant path; pSpike, population spike.

compared to those in the ventral DG. Our finding not only explains the reduced synaptic inhibition observed in the dorsal DG, but also supports both basket cells and several D-INs as the targets in the distant lamellae. On the other hand, the finding that the ventral MC → ventral GC connection is predominantly inhibitory supports a previous anatomical report showing that the primary targets of MCs in the hilus and subgranular zone are mostly INs (Buckmaster et al., 1996). Recently, a study reported that MCs preferentially target SST-INs, a classic type of D-INs, in the ventral lamella. Furthermore, a robust long-term potentiation can be induced at the MC → SST-IN synapses but not at the MC → GC synapses (Li et al., 2021). Collectively, these findings support a general view that inhibitory transmission is predominant at the ventral MC → ventral GC connection.

Reduced inhibition in the dorsal DG may contribute to the increased E/I balance in the dorsal GCs along the ventrodorsal (ventral DG → dorsal DG) pathway. Several pieces of evidence support this view. First, electron microscopy analysis of the MC axonal arborization showed that distant to the MC soma in the ipsilateral hippocampus, most biocytin-labelled MC terminals innervate GC dendrites, while only a few synapses in the IML make contact with INs (Buckmaster et al., 1996; Fredes et al., 2021). Similar results were also observed with the injection of biotinylated dextran amine (Fujise et al., 1998). Second, Bui et al. (2018) demonstrated that the photostimulation of ventral MCs leads to the increased activity of dorsal GCs using the juxtacellular recording in awake mice, in agreement with the observation that chemogenetic activation of ventral MC increased the c-Fos expression in dorsal GCs (Bauer et al., 2021; Fredes et al., 2021). Third, indirect evidence from behavioural studies supports the idea of the lamella-specific regulation of GC activities by MCs (Duffy et al., 2013). Notably, c-Fos analysis from mice exposed to a novel environment revealed an inverse relationship of c-Fos labelling between MCs and GCs along the dorsal–ventral axis of the hippocampus (Duffy et al., 2013). Specifically, c-Fos expression is high in ventral MCs and GCs in the dorsal hippocampus, but is low in GCs in the ventral hippocampus. Finally, a potential caveat is whether reduced inhibition or increased E/I balance observed in the dorsal DG is due to the cut of IN axons during slice preparation. Compared to excitation, which is mediated by monosynaptic connections, inhibition is mediated by di-synaptic connections and is likely to be more vulnerable to slice preparation. A recent study by Hsu et al. (2016) showed that the predominant inhibition is preserved in the slices while stimulating long-distance MC projections from the contralateral DG. MC commissural axonal projections target the same IML as the ventral MC associational axonal projections. Of note, the E/I balance is <1 at the dorsal MC commissural connection to dorsal GCs. Therefore, the possibility of reduced inhibition at the ventral MC → dorsal GC connection is unlikely due to the cut of inhibitory axons.

The major findings of this study support an earlier perspective that MCs can specialize in spreading excitation to dorsal GCs, while preventing hyperexcitability of ventral GCs, thereby maintaining the

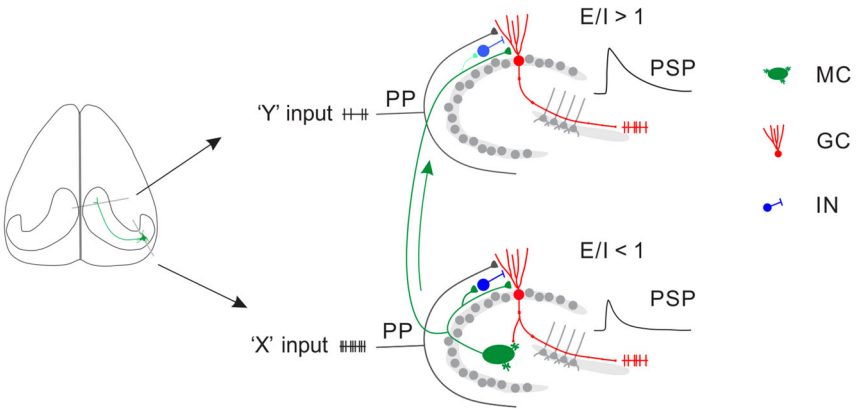

Figure 12. Synaptic effects of MC longitudinal projections on distant GCs
A schematic representation of ventral MC (green) projects a long axonal collateral to the dorsal DG and innervates GCs (red) and INs (blue). Salient 'X' input such as a novelty signal encoded by a pattern of spikes (hash marks) enters the ventral pole of the hippocampus via the PP fibres and activates ventral GCs (red). The ventral GC drives feedforward excitation to a ventral MC via its axonal collaterals. The ventral MC drives direct excitation and indirect inhibition to the ventral GC. Excitation of ventral MCs results in E/I <1 and therefore a fast PSP in a ventral GC. A weak 'Y' input such as contextual information, which enters the dorsal pole of the hippocampus via the PP fibres, modestly activates a GC in the dorsal DG. A ventral MC associational axonal collateral (a teaching signal) preferentially excites GCs (red) over INs (light blue) in the dorsal DG, resulting in E/I >1 and thus a slow PSP in a dorsal GC. DG, dentate gyrus; E/I, excitation/inhibition; GC, granule cell; IN, interneuron; MC, mossy cell; PP, perforant path; PSP, postsynaptic potential.

high threshold of the ventral DG (Buckmaster & Schwartzkroin, 1994; Scharfman, 2016; Scharfman & Myers, 2013). Consistent with this view, the predominant synaptic excitation at ventral MC → dorsal GC connections enables spatially separated subsets of dorsal GCs to associate with ventral GCs (Buckmaster & Schwartzkroin, 1994). Of note, our *in vivo* GC recordings support this view. Whether the E/I balance is affected along the dorsoventral (septotemporal) axis under pathological conditions, such as in temporal lobe epilepsy and traumatic brain injury, remains unknown. It is also worth mentioning that dorsal MCs and ventral MCs differ in their axonal projections throughout the DG of the mouse hippocampus (Botterill et al., 2021; Houser et al., 2021). Unlike ventral MC projections, which terminate in the IML, the dorsal MCs have a more diffuse distribution and expand into the MML in the ventral DG where they overlap and interact with innervation from the perforant path (Botterill et al., 2021; Houser et al., 2021; authors' unpublished observation). Our results revealed that dorsal MCs also form distinct connections with GCs and INs within the same and distant lamellae. However, in contrast to ventral MC → GC connections, IPSGs in local and distant GCs were equivalent in dorsal MC → GC connections, whereas the EPSG in distant GCs (i.e. ventral GCs) was significantly higher than that in local GCs (i.e. dorsal GCs). This finding indicated that the MCs mediate low E/I balance in local GCs and high E/I balance in distant GCs, regardless of the dorsoventral or ventrodorsal projections. However, whether the modulatory effects of MC dorsoventral pathways on action potential generation in GCs along the longitudinal axis are different from MC ventrodorsal pathways need to be investigated in future studies. Finally, we need to point out that the present study relies on artificial activation of MCs using the optogenetic approach. Whether synchronous activation of MCs can occur under physiological conditions remains an open question. New techniques that are capable of activating MCs in physiologically relevant stimulation patterns will further advance our knowledge about the functional connections of hilar MCs along the hippocampal longitudinal axis.

References

Ajibola, M. I., Wu, J. W., Abdulmajeed, W. I., & Lien, C. C. (2021). Hypothalamic glutamate/GABA cotransmission modulates hippocampal circuits and supports long-term potentiation. *Journal of Neuroscience*, **41**(39), 8181–8196.

Amaral, D. G. (1978). A Golgi study of cell types in the hilar region of the hippocampus in the rat. *Journal of Comparative Neurology*, **182**(5), 851–914.

Amaral, D. G., Scharfman, H. E., & Lavenex, P. (2007). The dentate gyrus: Fundamental neuroanatomical organization (dentate gyrus for dummies). *Progress in Brain Research*, **163**, 3–22.

Amaral, D. G., & Witter, M. P. (1989). The three-dimensional organization of the hippocampal formation: A review of anatomical data. *Neuroscience*, **31**(3), 571–591.

Bauer, J. P., Rader, S. L., Joffe, M. E., Kwon, W., Quay, J., Seanez, L., Zhou, C. P., Jeffrey Conn, P. J., & Lewis, A. S. (2021). Modeling intrahippocampal effects of anterior hippocampal hyperactivity relevant to schizophrenia using chemogenetic excitation of long axis–projecting mossy cells in the mouse dentate gyrus. *Biological Psychiatry: Global Open Science*, **1**, 101–111.

Blasco-Ibáñez, J. M., & Freund, T. F. (1997). Distribution, ultrastructure, and connectivity of calretinin-immunoreactive mossy cells of the mouse dentate gyrus. *Hippocampus*, **7**(3), 307–320.

Botterill, J. J., Lu, Y. L., LaFrancois, J. J., Bernstein, H. L., Alcantara-Gonzalez, D., Jain, S., Leary, P., & Scharfman, H. E. (2019). An excitatory and epileptogenic effect of dentate gyrus mossy cells in a mouse model of epilepsy. *Cell Reports*, **29**(9), 2875–2889.e6.

Botterill, J. J., Gerencer, K. J., Vinod, K. Y., Alcantara-Gonzalez, D., & Scharfman, H. E. (2021). Dorsal and ventral mossy cells differ in their axonal projections throughout the dentate gyrus of the mouse hippocampus. *Hippocampus*, **31**(5), 522–539.

Buckmaster, P. S., & Schwartzkroin, P. A. (1994). Hippocampal mossy cell function: A speculative view. *Hippocampus*, **4**(4), 393–402.

Buckmaster, P. S., Strowbridge, B. W., Kunkel, D. D., Schmiege, D. L., & Schwartzkroin, P. A. (1992). Mossy cell axonal projections to the dentate gyrus molecular layer in the rat hippocampal slice. *Hippocampus*, **2**(4), 349–362.

Buckmaster, P. S., Wenzel, H. J., Kunkel, D. D., & Schwartzkroin, P. A. (1996). Axon arbors and synaptic connections of hippocampal mossy cells in the rat in vivo. *Journal of Comparative Neurology*, **366**(2), 270–292.

Bui, A. D., Nguyen, T. M., Limouse, C., Kim, H. K., Szabo, G. G., Felong, S., Maroso, M., & Soltesz, I. (2018). Dentate gyrus mossy cells control spontaneous convulsive seizures and spatial memory. *Science*, **359**(6377), 787–790.

Butler, C. R., Westbrook, G. L., & Schnell, E. (2022). Adaptive mossy cell circuit plasticity after status epilepticus. *Journal of Neuroscience*, **42**(14), 3025–3036.

Diamantaki, M., Frey, M., Berens, P., Preston-Ferrer, P., & Burgalossi, A. (2016). Sparse activity of identified dentate granule cells during spatial exploration. *eLife*, **5**, e20252.

Duffy, A. M., Schaner, M. J., Chin, J., & Scharfman, H. E. (2013). Expression of c-fos in hilar mossy cells of the dentate gyrus *in vivo*. *Hippocampus*, **23**(8), 649–655.

Engen, H. G., & Anderson, M. C. (2018). Memory control: A fundamental mechanism of emotion regulation. *Trends in Cognitive Sciences*, **22**(11), 982–995.

Ewell, L. A., & Jones, M. V. (2010). Frequency-tuned distribution of inhibition in the dentate gyrus. *Journal of Neuroscience*, **30**(38), 12597–12607.

Fanselow, M. S., & Dong, H. W. (2010). Are the dorsal and ventral hippocampus functionally distinct structures? *Neuron*, **65**(1), 7–19.

Femenía, T., Gómez-Galán, M., Lindskog, M., & Magara, S. (2012). Dysfunctional hippocampal activity affects emotion and cognition in mood disorders. *Brain Research*, **1476**, 58–70.

Fredes, F., & Shigemoto, R. (2021). The role of hippocampal mossy cells in novelty detection. *Neurobiology of Learning and Memory*, **183**, 107486.

Fredes, F., Silva, M. A., Koppensteiner, P., Kobayashi, K., Joesch, M., & Shigemoto, R. (2021). Ventro-dorsal hippocampal pathway gates novelty-induced contextual memory formation. *Current Biology*, **31**(1), 25–38.e5.

Freund, T. F., & Buzsáki, G. (1996). Interneurons of the hippocampus. *Hippocampus*, **6**(4), 347–470.

Fujise, N., & Kosaka, T. (1999). Mossy cells in the mouse dentate gyrus: Identification in the dorsal hilus and their distribution along the dorsoventral axis. *Brain Research*, **816**(2), 500–511.

Fujise, N., Liu, Y., Hori, N., & Kosaka, T. (1998). Distribution of calretinin immunoreactivity in the mouse dentate gyrus: II. Mossy cells, with special reference to their dorsoventral difference in calretinin immunoreactivity. *Neuroscience*, **82**(1), 181–200.

GoodSmith, D., Chen, X., Wang, C., Kim, S. H., Song, H., Burgalossi, A., Christian, K. M., & Knierim, J. J. (2017). Spatial representations of granule cells and mossy cells of the dentate gyrus. *Neuron*, **93**(3), 677–690.e5.

Hashimotodani, Y., Nasrallah, K., Jensen, K. R., Chávez, A. E., Carrera, D., & Castillo, P. E. (2017). LTP at hilar mossy cell-dentate granule cell synapses modulates dentate gyrus output by increasing excitation/inhibition balance. *Neuron*, **95**(4), 928–943.e3.

Henze, D. A., & Buzsáki, G. (2007). Hilar mossy cells: Functional identification and activity *in vivo*. *Progress in Brain Research*, **163**, 199–216.

Hosp, J. A., Struber, M., Yanagawa, Y., Obata, K., Vida, I., Jonas, P., & Bartos, M. (2014). Morpho-physiological criteria divide dentate gyrus interneurons into classes. *Hippocampus*, **24**(2), 189–203.

Houser, C. R., Peng, Z., Wei, X., Huang, C. S., & Mody, I. (2021). Mossy cells in the dorsal and ventral dentate gyrus differ in their patterns of axonal projections. *Journal of Neuroscience*, **41**(5), 991–1004.

Hsu, T. T., Lee, C. T., Tai, M. H., & Lien, C. C. (2016). Differential recruitment of dentate gyrus interneuron types by commissural versus perforant pathways. *Cerebral Cortex*, **26**(6), 2715–2727.

Hutcheon, B., & Yarom, Y. (2000). Resonance, oscillation and the intrinsic frequency preferences of neurons. *Trends in Neuroscience*, **23**(5), 216–222.

Hu, H., Vervaeke, K., Graham, L. J., & Storm, J. F. (2009). Complementary theta resonance filtering by two spatially segregated mechanisms in CA1 hippocampal pyramidal neurons. *Journal of Neuroscience*, **29**(46), 14472–14483.

Jeewajee, A., Barry, C., O'Keefe, J., & Burgess, N. (2008). Grid cells and theta as oscillatory interference: Electrophysiological data from freely moving rats. *Hippocampus*, **18**(12), 1175–1185.

Jinde, S., Zsiros, V., Jiang, Z., Nakao, K., Pickel, J., Kohno, K., Belforte, J. E., & Nakazawa, K. (2012). Hilar mossy cell degeneration causes transient dentate granule cell hyperexcitability and impaired pattern separation. *Neuron*, **76**(6), 1189–1200.

Jinde, S., Zsiros, V., & Nakazawa, K. (2013). Hilar mossy cell circuitry controlling dentate granule cell excitability. *Frontiers in Neural Circuits*, **7**, 14.

Jinno, S., Ishizuka, S., & Kosaka, T. (2003). Ionic currents underlying rhythmic bursting of ventral mossy cells in the developing mouse dentate gyrus. *European Journal of Neuroscience*, **17**(7), 1338–1354.

Larimer, P., & Strowbridge, B. W. (2008). Nonrandom local circuits in the dentate gyrus. *Journal of Neuroscience*, **28**(47), 12212–12223.

Lee, C. T., Kao, M. H., Hou, W. H., Wei, Y. T., Chen, C. L., & Lien, C. C. (2016). Causal evidence for the role of specific GABAergic interneuron types in entorhinal recruitment of dentate granule cells. *Science Reports*, **6**(1), 36885.

Lee, S., Kruglikov, I., Huang, Z. J., Fishell, G., & Rudy, B. (2013). A disinhibitory circuit mediates motor integration in the somatosensory cortex. *Nature Neuroscience*, **16**(11), 1662–1670.

Li, X., Chen, W., Yu, Q., Zhang, Q., Zhang, T., Huang, X., Li, H., He, A., Yu, H., Jing, W., Du, H., Ke, X., Zhang, B., Tian, Q., Liu, R., & Lu, Y. (2021). A circuit of mossy cells controls the efficacy of memory retrieval by Gria2I inhibition of Gria2. *Cell Reports*, **34**(7), 108741.

Lien, C. C., & Jonas, P. (2003). Kv3 potassium conductance is necessary and kinetically optimized for high-frequency action potential generation in hippocampal interneurons. *Journal of Neuroscience*, **23**(6), 2058–2068.

Liu, Y. C., Cheng, J. K., & Lien, C. C. (2014). Rapid dynamic changes of dendritic inhibition in the dentate gyrus by presynaptic activity patterns. *Journal of Neuroscience*, **34**(4), 1344–1357.

Milstein, A. D., & Soltesz, I. (2017). Hippocampal dentate mossy cells improve their CV and Trk into the limelight. *Neuron*, **95**(4), 732–734.

O'Keefe, J. (1999). Do hippocampal pyramidal cells signal non-spatial as well as spatial information? *Hippocampus*, **9**(4), 352–364.

Paxinos, G., & Franklin, K. B. J. (2001). *The mouse brain in stereotaxic coordinates* (2nd edn.). Academic Press, Elsevier Publishing, San Diego, CA, USA.

Pernía-Andrade, A. J., & Jonas, P. (2014). Theta-gamma-modulated synaptic currents in hippocampal granule cells in vivo define a mechanism for network oscillations. *Neuron*, **81**(1), 140–152.

Pinault, D. (1996). A novel single-cell staining procedure performed in vivo under electrophysiological control: Morpho-functional features of juxtacellularly labeled thalamic cells and other central neurons with biocytin or Neurobiotin. *Journal of Neuroscience Methods*, **65**(2), 113–136.

Pouille, F., & Scanziani, M. (2001). Enforcement of temporal fidelity in pyramidal cells by somatic feed-forward inhibition. *Science*, **293**(5532), 1159–1163.

Scharfman, H. E. (1995). Electrophysiological evidence that dentate hilar mossy cells are excitatory and innervate both granule cells and interneurons. *Journal of Neurophysiology*, **74**(1), 179–194.
Scharfman, H. E. (2016). The enigmatic mossy cell of the dentate gyrus. *Nature Reviews. Neuroscience*, **17**(9), 562–575.
Scharfman, H. E., & Myers, C. E. (2013). Hilar mossy cells of the dentate gyrus: A historical perspective. *Frontiers in Neural Circuits*, **6**, 106.
Scharfman, H. E. (2007). *The dentate gyrus: Comprehensive guide to structure, function and clinical implications* (Vol. **163**). Elsevier.
Schindelin, J., Arganda-carreras, I., Frise, E., Kaynig, V., Longair, M., Pietzsch, T., Preibisch, S., Rueden, C., Saalfeld, S., Schmid, B., Tinevez, J., White, D. J., Hartenstein, V., Eliceiri, K., Tomancak, P., & Cardona, A. (2012). Fiji: An open-source platform for biological-image analysis. *Nature Methods*, **9**(7), 676–682.
Senzai, Y., & Buzsáki, G. (2017). Physiological properties and behavioral correlates of hippocampal granule cells and mossy cells. *Neuron*, **93**(3), 691–704.e5.
Soltesz, I., Bourassa, J., & Deschênes, M. (1993). The behavior of mossy cells of the rat dentate gyrus during theta oscillations in vivo. *Neuroscience*, **57**(3), 555–564.
Strange, B. A., Witter, M. P., Lein, E. S., & Moser, E. I. (2014). Functional organization of the hippocampal longitudinal axis. *Nature Reviews. Neuroscience*, **15**(10), 655–669.
Swaminathan, A., Wichert, I., Schmitz, D., & Maier, N. (2018). Involvement of mossy cells in sharp wave-ripple activity in vitro. *Cell Reports*, **23**(9), 2541–2549.
Tavares, R. M., Mendelsohn, A., Grossman, Y., Williams, C. H., Shapiro, M., Trope, Y., & Schiller, D. (2015). A map for social navigation in the human brain. *Neuron*, **87**(1), 231–243.
Temprana, S. G., Mongiat, L. A., Yang, S. M., Trinchero, M. F., Alvarez, D. D., Kropff, E., Giacomini, D., Beltramone, N., Lanuza, G. M., & Schinder, A. F. (2015). Delayed coupling to feedback inhibition during a critical period for the integration of adult-born granule cells. *Neuron*, **85**(1), 116–130.
Wang, K. Y., Wu, J. W., Cheng, J. K., Chen, C. C., Wong, W. Y., Averkin, R. G., Tamás, G., Nakazawa, K., & Lien, C. C. (2021). Elevation of hilar mossy cell activity suppresses hippocampal excitability and avoidance behavior. *Cell Reports*, **36**(11), 109702.
Yeh, C. Y., Asrican, B., Moss, J., Quintanilla, L. J., He, T., Mao, X., Cassé, F., Gebara, E., Bao, H., Lu, W., Toni, N., & Song, J. (2018). Mossy cells control adult neural stem cell quiescence and maintenance through a dynamic balance between direct and indirect pathways. *Neuron*, **99**(3), 493–510.e4.

Additional information

Data availability statement

Data will be made available upon reasonable request to the corresponding author.

Competing interests

The authors declare no competing interest.

Author contributions

W.I.A., K.Y.W. and M.I.A. performed the *ex vivo* slice recordings. K.Y.W. performed the *in vivo* juxtacellular recordings. W.I.A. and J.W.W. analysed the data. W.I.A., I.H.C. and C.C.L. conceptualized the project. W.I.A. and C.C.L. wrote the paper and C.C.L. acquired the funding. All authors revised the paper. All authors have read and approved the final version of this manuscript and agree to be accountable for all aspects of the work in ensuring that questions related to the accuracy or integrity of any part of the work are appropriately investigated and resolved. All persons designated as authors qualify for authorship, and all those who qualify for authorship are listed.

Funding

This work was financially supported by the National Health Research Institutes (NHRI-EX111-11135NI), Ministry of Science and Technology (MOST 108-2320-B-010-026-MY3, 109-2926-I-010-506, 110-2321-B-010-006, 111-2321-B-A49-005, and Shackleton Scholar Program 108-2638-B-010-002-MY2), and Brain Research Center, National Yang Ming Chiao Tung University from the Featured Areas Research Center Program within the framework of the Higher Education Sprout Project by the Ministry of Education in Taiwan.

Acknowledgements

The authors thank Dominique Engel and Kazu Nakazawa for commenting on earlier versions of the manuscript and the members of the Lien Lab for the insightful discussions.

Keywords

dentate gyrus, electrophysiology, GABA, hippocampus, inetrneuron, mossy cell, optogenetics, synapse

Supporting information

Additional supporting information can be found online in the Supporting Information section at the end of the HTML view of the article. Supporting information files available:

Peer Review History
Statistical Summary Document